The Planetary Science Journal, 6:54 (17pp), 2025 March https://doi.org/10.3847/PSJ/ada778

Measuring the Effects of Regolith Porosity on Mid-IR Spectra of the Allende Meteorite

Lonnie D. Dausend[1], Audrey C. Martin[2], and Joshua P. Emery[1]

[1] Department of Astronomy and Planetary Science, Northern Arizona University, Flagstaff, Arizona, 86011, USA; ldd68@nau.edu

[2] Department of Physics, University of Central Florida, Orlando, Florida, 32816, USA

Received 2024 August 1; revised 2024 December 24; accepted 2025 January 3; published 2025 March 4

Abstract

Mid-infrared (MIR; 5–35 μm) spectroscopy of laboratory meteorites does not often match asteroid spectra, making it difficult to constrain the parent bodies of meteorites using the MIR. To potentially improve the number of meteorite–asteroid matches, we simulated the effects of regolith porosity on the MIR spectra of the Allende meteorite. We separated a sample of Allende into three particle sizes (<63 μm) and mixed them with various amounts of potassium bromide (KBr). We then collected MIR spectra of the KBr-mixed Allende samples, defined spectral features that may be indicative of composition and regolith porosity, and analyzed how the parameters of the spectral features (e.g., position and spectral contrast) changed with increasing regolith porosity. The Allende spectra show a transition from surface scattering to volume scattering as regolith porosity increases. Comparing to an olivine sample analyzed the same way shows that the opaque minerals in Allende may not have a significant effect on regolith porosity in the MIR. Finally, we present the MIR spectral analysis of four asteroids measured from the Spitzer Space Telescope: (114) Kassandra, (234) Barbara, (5261) Eureka, and (85989) 1999 JD_6. We find that Kassandra and Barbara have high total porosities with some evidence of olivine, and Eureka and 1999 JD_6 have low total porosities, with Eureka having strong evidence of olivine and 1999 JD_6 having little evidence of olivine. This work shows how measuring MIR spectra of KBr-diluted particulate meteorites improves our ability to interpret the surface compositions and regoliths of asteroids from telescopic MIR spectra.

Unified Astronomy Thesaurus concepts: Meteorites (1038); Carbonaceous chondrites (200); Asteroids (72); Spectral energy distribution (2129); Infrared spectroscopy (2285); Spectroscopy (1558); Asteroid surfaces (2209)

1. Introduction

Mid-infrared (MIR; 5–35 μm) spectroscopy is an important tool for shedding light on the history of the solar system. By examining the MIR spectra of asteroids, their surface compositions can be constrained, which can reveal information about the formation and evolution of the solar system (e.g., B. Yang et al. 2013; P. Vernazza et al. 2017; A. C. Martin & J. P. Emery 2023). As many meteorites are sourced directly from asteroids, linking them to their parent asteroid can provide unique insights into early solar system processes. However, very few meteorites have been linked to specific asteroids or asteroid families. Only 95–148 out of the ~62,000 meteorites in the global collection have been linked to possible parent bodies (R. C. Greenwood et al. 2020), with asteroid 4 Vesta and the howardite–eucrite–diogenite meteorites being the only near-certain linkage (e.g., T. B. McCord et al. 1970; H. Y. McSween et al. 2013). Furthermore, laboratory spectra of meteorites do not provide perfect matches for asteroids in the MIR (e.g., J. P. Emery et al. 2006; P. Vernazza et al. 2012; M. M. McAdam et al. 2015; A. Morlok et al. 2020). This is likely due, in part, to the MIR portion of the electromagnetic spectrum being affected by many factors, such as chemical composition, particle size, regolith porosity, mineral structure (crystalline versus amorphous), and environmental conditions that can be altered when taking laboratory measurements (e.g., J. W. Salisbury & A. Wald 1992; J. R. Brucato et al. 2004; V. E. Hamilton 2010; P. Vernazza et al. 2012; K. L. Donaldson Hanna et al. 2017; C. Lantz et al. 2017; A. C. Martin et al. 2022, 2023). Therefore, examining the complexities of MIR spectra leads to better interpretations of asteroid spectra and could potentially increase the number of known parent bodies for meteorites.

1.1. Background

Visible and near-infrared (VNIR; 0.4–2.5 μm) spectroscopy has been used to both constrain the surface composition of asteroids (e.g., J. M. Sunshine et al. 2008; J. P. Emery et al. 2011; J. A. Sanchez et al. 2014; J. Gomez Barrientos et al. 2024) and to link asteroids to meteorites (e.g., B. E. Clark et al. 2009; J. Eschrig et al. 2021; F. E. DeMeo et al. 2022). However, linking meteorites to a specific asteroid based on VNIR spectroscopy alone has limitations. Many asteroids have similar or no spectral features in the VNIR, so meteorites are typically linked to a spectral class, as opposed to a single asteroid (R. C. Greenwood et al. 2020). Conversely, the MIR spectra of asteroids exhibit more spectral diversity than in the VNIR (e.g., P. Vernazza et al. 2010; F. Marchis et al. 2012). Therefore, it may be possible to link a meteorite to a single asteroid or a more constrained number of asteroids using MIR spectroscopy.

In this paper, we perform a study of the MIR spectra of the CV 3 Allende meteorite. CV 3 chondrites are generally characterized by large amounts of olivine, large chondrules with respect to the matrix, and abundant opaque minerals (e.g., H. Y. J. McSween 1977; K. T. Howard et al. 2010). Embedded within CV 3 chondrites are calcium-aluminum-rich inclusions (CAIs; e.g., U. B. Marvin et al. 1970; J. M. Sunshine et al. 2008), which are the first minerals to condense from the solar nebula (H. C. Lord 1965). Carbonaceous chondrites therefore contain a record of the early solar system, making them good analogs for primitive asteroids.

Allende's mineralogy has been determined using methods such as X-ray diffraction, backscattered scanning electron microscopy, and spectroscopy (e.g., R. S. J. Clarke et al. 1971; A. S. Kornacki & J. A. Wood 1984; W. F. Müller et al. 1995; K. T. Howard et al. 2010). Excluding large inclusions such as CAIs, Allende consists of 82.7–83.9 vol% olivine, 6.3–6.6 vol% enstatite, 6.6–8.0 vol% sulfide, and other minerals (P. A. Bland et al. 2004; K. T. Howard et al. 2010). CAIs make up 9.4 vol% in Allende (H. Y. J. McSween 1977), and are separated into two types: type A and type B. Type A CAIs contain 80%–85% melilite, 15%–20% spinel, and 1%–2% perovskite; type Bs contain 35%–60% clinopyroxene, 15%–30% spinel, 5%–25% plagioclase, and 5%–20% melilite (L. Grossman 1975). Carbonaceous material in Allende is about 0.18 wt% (C. M. O. D. Alexander et al. 2007). For a review on the physical and spectral (VNIR) properties of Allende and CV 3 chondrites, see E. A. Cloutis et al. (2012).

As Allende is primarily composed of olivine (e.g., P. A. Bland et al. 2004), MIR spectra of Allende strongly resemble olivine spectra (e.g., P. Beck et al. 2014). The MIR spectra of silicate minerals are affected by their Mg# (i.e., Mg/[Mg+Fe]), which is a useful indicator of the formation region of silicates in the solar system (e.g., H. P. Gail 2004; T. Henning 2010). Mg-rich silicates tended to form in the inner solar system, and Fe-rich silicates tended to form in the outer solar system. With decreasing Mg# (increasing Fe content), many spectral features of olivines and pyroxenes shift to longer wavelengths (e.g., V. E. Hamilton 2000, 2010; H. Chihara et al. 2002; C. Koike et al. 2003). Therefore, the formation region of small solar system bodies bearing silicates can be constrained based on MIR spectra.

In addition to mineralogy and mineral composition, MIR spectra are also dependent on the scattering regime. Surface-scattering dominates when particles are coarse ($\geqslant 65\,\mu$m) and have very low regolith porosities (e.g., J. W. Salisbury & J. W. Eastes 1985; J. W. Salisbury & A. Wald 1992; V. E. Hamilton 2010). Conversely, the volume-scattering regime dominates when particles are small and regolith porosity is high. The scattering regime has various effects on the spectral features of a mineral's MIR spectrum (e.g., J. F. Mustard & J. E. Hays 1997; P. Vernazza et al. 2012; M. R. M. Izawa et al. 2021; A. C. Martin et al. 2022, 2023).

Important spectral features used for composition characterization include reststrahlen bands (RBs), Christiansen features (CFs), and the transparency feature (TF; J. W. Salisbury et al. 1991). RBs are features caused by the Si–O fundamental vibrational modes of silicates and occur at wavelengths where the absorption coefficient is high. These features appear as emissivity minima (reflectance maxima) and can exhibit large spectral contrast in the surface-scattering regime. CFs are well-defined emissivity maxima that occur when the real portion of the refractive index of a mineral approaches that of the surrounding medium, and they are located on the short-wavelength side of RBs. In the spectrum of olivine, a primary CF (CF_1) occurs at $\sim 9\,\mu$m, and a secondary CF (CF_2) occurs near $15\,\mu$m (e.g., V. E. Hamilton 2010; M. D. Lane et al. 2011). TFs are volume-scattering features that appear as emissivity minima where absorption coefficients are low, and one usually occurs between RBs at $\sim 13\,\mu$m for silicates.

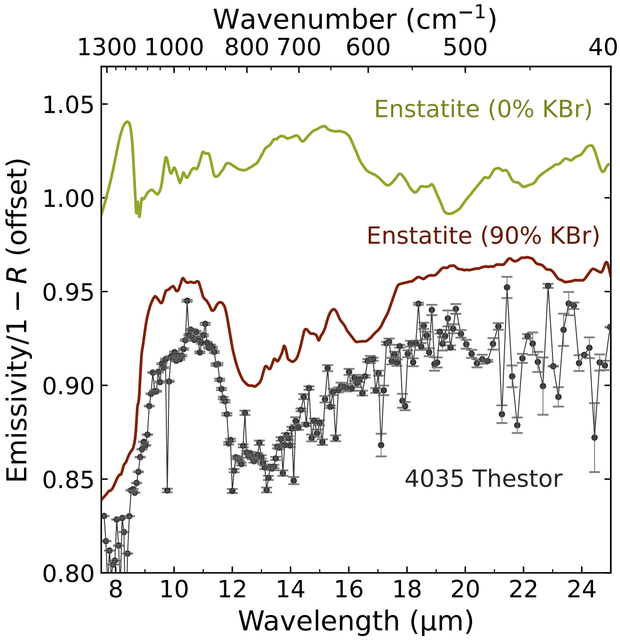

Figure 1. Comparison of reflectance (R) spectra (converted to emissivity via Kirchhoff's law) of two enstatite samples from A. C. Martin et al. (2023) with different scattering regimes to the emissivity spectrum of an airless body. The top spectrum (green) is of an enstatite ($\mathrm{Mg}_{89.7}$) sample with 0 wt% KBr with a particle size range of 45–63 μm, and is primarily in the surface-scattering regime. The middle spectrum (red) is of the same 45–63 μm enstatite sample as above, but with 90 wt% KBr mixed in to simulate regolith porosity, and represents a spectrum dominated by volume-scattering. Both enstatite spectra are scaled by 0.72 and are offset for clarity. The bottom spectrum (black) is asteroid (4035) Thestor from A. C. Martin & J. P. Emery (2023) observed with the Spitzer Space Telescope. The enstatite spectrum with 90% KBr better resembles the spectrum of Thestor than the enstatite spectrum with no KBr, indicating that Thestor's MIR spectrum may be dominated by volume-scattering.

As volume-scattering begins to dominate, RBs reduce in spectral contrast and may invert to become emissivity maxima, while CFs shift to longer wavelengths and reduce in spectral contrast, and TFs increase in spectral contrast (e.g., G. R. Hunt & L. M. Logan 1972; J. F. Mustard & J. E. Hays 1997; C. L. Young et al. 2019; A. C. Martin et al. 2022, 2023). The MIR spectra of many asteroids—such as the Jupiter Trojans—show signs of volume-scattering (e.g., J. P. Emery et al. 2006; P. Vernazza et al. 2012; B. Yang et al. 2013; V. C. Lowry et al. 2022; A. C. Martin et al. 2022, 2023; A. C. Martin & J. P. Emery 2023; R. Sultana et al. 2023). Furthermore, numerous studies have shown that the spectra of some asteroids are better modeled by minerals mixed with MIR-transparent material such as potassium bromide (KBr), such as the spectra shown in Figure 1 (e.g., P. Vernazza et al. 2012; B. Yang et al. 2013; C. L. Young et al. 2019; A. C. Martin et al. 2022, 2023; A. C. Martin & J. P. Emery 2023). It is therefore important to understand the effect that volume scattering has on the MIR spectrum of meteorites like Allende to aid in identifying a potential parent body.

In this paper, we investigate the spectral properties of fine-particulate ($<63\,\mu$m) Allende powders mixed with KBr (a proxy for regolith porosity), building on results from A. C. Martin et al. (2022, 2023). Specifically, we investigate (1) how MIR spectra of powdered Allende are affected by regolith porosity and particle size, (2) the utility of end-member MIR spectra for identifying constituent minerals present in

Table 1
EMP Silicate Compositional Data (wt% Oxide), Averaged Over Many Grains

Oxide	Olivine	Clinopyroxene	Orthopyroxene
SiO_2	38.58	51.35	57.15
TiO_2	0.06	1.61	0.22
Al_2O_3	0.40	4.99	1.40
Cr_2O_3	0.30	0.52	0.62
Fe_2O_3	n.d.	n.d.	n.d.
FeO	19.11	1.21	3.03
MnO	0.16	0.11	0.14
MgO	39.76	20.39	35.83
CaO	0.28	19.32	1.09
Na_2O	n.d.	0.07	0.02
Total	98.65	99.58	99.50

Note. All Fe calculated as Fe^{+2}. Values at 0.00% are not detected (n.d.).

Allende at different regolith porosities, and (3) the utility of our Allende spectra for assessing the composition and regolith porosity of airless bodies.

2. Methodology

2.1. Sample Suite

The sample of Allende we used in our study came from Peter Wasilewski at NASA Goddard Space Flight Center, who retrieved the sample from the National Science Museum. We used a Cameca SX-100 electron microprobe (EMP) at the University of Tennessee to perform a petrologic analysis on our sample (Table 1). As Allende is heterogeneous, we analyzed a thick section of a sample of the Allende powder investigated spectroscopically in this study and determined representative mineral compositions. The analysis was done with an accelerating potential of 15 keV, a beam current of 20 nA, and a 1–5 μm beam size. Our Allende sample is dominated by a variety of olivine compositions ($Mg_{40–99}$). Pyroxene compositions are very iron-poor ($Mg_{93–99}$), and include various amounts of enstatite, diopside, and augite.

2.2. Sample Preparation and Measurement

To prepare our samples, we first ground the Allende meteorite into a fine-particulate powder using a small agate mortar and pestle. Using a Gilson Performer III Sieve Shaker, we sieved the powder into three particle size ranges: 0–20, 20–45, and 45–63 μm. We then mixed the samples in each size bin with KBr, which was also ground and sieved to the same particle sizes. We used KBr as a proxy for regolith porosity because it is an MIR-transparent material (e.g., P. Vernazza et al. 2012; A. C. Martin et al. 2022, 2023). Each Allende sample was mixed with 0%–90% KBr by wt%, in 10 wt% increments, resulting in 10 samples for each particle size fraction. Before mixing the samples, we weighed both the Allende and KBr portions to calculate the fraction of both Allende and KBr to the total mass of Allende and KBr. We define f_{ALD} as the fraction of Allende to the total mass, and f_{KBr} is the fraction of KBr to the total mass. Throughout the rest of this paper, we will refer to the wt% of KBr (i.e., $f_{\mathrm{KBr}} \cdot 100\%$) as "regolith porosity" to be consistent with previous authors (e.g., M. R. M. Izawa et al. 2021; A. C. Martin et al. 2022, 2023).

For spectral measurements, we poured each sample into PIKE Technologies sample cups. Two sample cups were used for our measurements: a large cup (0.18 cm^3) and a small cup (0.03 cm^3). When possible, we used the large cup to maximize measurement surface area. Sample cups were lightly tapped as they were filled, and a straight edge razor was used to level the top. We measured the mass of each sample cup before and after filling it with a sample for regolith porosity calculations.

Next, we calculated the total porosity of the sample (Φ), which is the ratio of the volume of air (V_{air}) plus the volume of KBr (V_{KBr}) within the cup to the total volume of the sample cup ($V_{\mathrm{sample\ cup}}$; not to be confused with "regolith porosity," which is strictly the contribution due to KBr). The volume of KBr is given by

$$V_{\mathrm{KBr}} = f_{\mathrm{KBr}} \frac{m_{\mathrm{sample}}}{\rho_{\mathrm{KBr}}}, \tag{1}$$

where m_{sample} is the total mass of the sample in the sample cup after weighing it, and ρ_{KBr} is the density of KBr. The volume of Allende (V_{ALD}) was calculated using Equation (1) and replacing f_{KBr} and ρ_{KBr} with f_{ALD} and ρ_{ALD}, respectively. We used densities of $\rho_{\mathrm{KBr}} = 2.75$ g cm^{-3} and $\rho_{\mathrm{ALD}} = 3.65$ g cm^{-3} (K. T. Howard et al. 2010; R. J. Macke et al. 2011). The volume of air is the volume within the sample cup not occupied by the sample (i.e., $V_{\mathrm{air}} = V_{\mathrm{sample\ cup}} - [V_{\mathrm{ALD}} + V_{\mathrm{KBr}}]$). Thus, the total porosity is given by

$$\begin{aligned} \Phi &= \frac{V_{\mathrm{air}} + V_{\mathrm{KBr}}}{V_{\mathrm{sample\ cup}}} \\ &= 1 - \frac{V_{\mathrm{ALD}}}{V_{\mathrm{sample\ cup}}}, \end{aligned} \tag{2}$$

and values are provided in Table 2.

We will refer to each Allende sample using the abbreviation $\mathrm{ALD}_{a,b}$, where a denotes the particle size of the sample, in which S, M, and L represent the 0–20, 20–45, and 45–63 μm particle sizes, respectively, and b denotes the approximate regolith porosity (wt% KBr) in the sample. For example, $\mathrm{ALD}_{M,30}$ refers to the 20–45 μm sample with 70% Allende and 30% regolith porosity. We did not have enough of the 45–63 μm samples to make any measurements for $\mathrm{ALD}_{L,0}$, so there are 29 total samples.

For spectral measurements, we placed each sample cup into a Thermo-Nicolet IS50 Fourier transform infrared (FTIR) spectrometer. A PIKE Technologies EasiDiff diffuse reflectance accessory was utilized, and the reflectance spectrum was an average of 300 scans between 4000 and 400 cm^{-1} (2.5–25 μm) at a 4 cm^{-1} spectral sampling. Atmospheric effects were reduced by taking the spectrum of pure KBr for each particle size and dividing our sample spectra by it. Finally, we converted from reflectance (R) to emissivity (ε) using Kirchhoff's law: $\varepsilon \cong 1–R$. We note that Kirchhoff's law strictly applies to hemispherical reflectance. For diffuse reflectance, the positions, shapes, and relative sizes of bands are not significantly affected (e.g., J. W. Salisbury et al. 1991).

3. Results

3.1. MIR Spectra

The spectra of the lowest regolith porosity samples (i.e., $\mathrm{ALD}_{S,0}$, $\mathrm{ALD}_{M,0}$, and $\mathrm{ALD}_{L,10}$) share many similar spectral characteristics (Figure 2), and there are several spectral features shortward of 12 μm that are important indicators of mineralogy. There is a broad peak near 9 μm that is a combination of two smaller peaks (P_1 at ~8.59 μm and P_2 at ~9.11 μm). There

Table 2
Volume and Porosity Measurements of the Allende Samples

Sample	f_{KBr}	V_{ALD}	V_{KBr}	V_{air}	Φ
$\mathrm{ALD}_{S,0}$	0.00	32.76	0.00	67.24	67.24
$\mathrm{ALD}_{S,10}$	10.00	28.03	4.15	67.83	71.97
$\mathrm{ALD}_{S,20}$	20.20	23.66	7.93	68.41	76.34
$\mathrm{ALD}_{S,30}$	29.77	22.23	12.52	65.25	77.77
$\mathrm{ALD}_{S,40}$	40.13	16.96	15.11	67.93	83.04
$\mathrm{ALD}_{S,50}$	50.00	15.01	19.93	65.06	84.99
$\mathrm{ALD}_{S,60}$	59.80	9.98	19.74	70.28	90.02
$\mathrm{ALD}_{S,70}$	70.13	8.22	25.70	66.09	91.78
$\mathrm{ALD}_{S,80}$	80.00	5.27	27.70	67.03	94.73
$\mathrm{ALD}_{S,90}$	89.70	2.44	29.07	68.49	97.56
$\mathrm{ALD}_{M,0}$	0.00	39.74	0.00	60.26	60.26
$\mathrm{ALD}_{M,10}$	9.97	32.35	4.76	62.89	67.65
$\mathrm{ALD}_{M,20}$	19.73	31.38	10.25	58.37	68.62
$\mathrm{ALD}_{M,30}$	30.00	25.40	14.49	60.11	74.60
$\mathrm{ALD}_{M,40}$	40.07	22.22	19.76	58.02	77.78
$\mathrm{ALD}_{M,50}$	49.83	17.53	23.27	59.19	82.47
$\mathrm{ALD}_{M,60}$	59.80	14.64	29.01	56.34	85.36
$\mathrm{ALD}_{M,70}$	69.77	10.74	33.14	56.12	89.26
$\mathrm{ALD}_{M,80}$	80.20	7.36	39.72	52.92	92.64
$\mathrm{ALD}_{M,90}$	90.00	3.13	37.50	59.37	96.87
$\mathrm{ALD}_{L,10}$	10.26	35.88	5.41	58.70	64.12
$\mathrm{ALD}_{L,20}$	20.33	31.65	10.64	57.71	68.35
$\mathrm{ALD}_{L,30}$	29.90	26.75	15.17	58.08	73.25
$\mathrm{ALD}_{L,40}$	39.93	23.43	20.74	55.83	76.57
$\mathrm{ALD}_{L,50}$	50.17	18.95	25.15	55.91	81.05
$\mathrm{ALD}_{L,60}$	59.87	15.38	30.61	54.01	84.62
$\mathrm{ALD}_{L,70}$	70.00	10.84	33.68	55.48	89.16
$\mathrm{ALD}_{L,80}$	80.27	7.31	38.29	54.40	92.69
$\mathrm{ALD}_{L,90}$	90.30	3.69	43.08	53.23	96.31

Note. f_{KBr} is the regolith porosity in wt% KBr. V_{ALD}, V_{KBr}, V_{air}, and Φ are in vol%. As the volumes are provided in vol%, the volumes in cm^3 can be found by multiplying by the total volume (i.e., $V_{\mathrm{sample\ cup}}$).

is a large dip at ∼10.83 μm (D_4) that is round in the $\mathrm{ALD}_{S,0}$ spectrum, but sharper in both the $\mathrm{ALD}_{M,0}$ and $\mathrm{ALD}_{L,10}$ spectra. Longward of 12 μm, there is a small dip at ∼12.36 μm (D_7) in the $\mathrm{ALD}_{S,0}$ spectrum, but it is absent in the $\mathrm{ALD}_{M,0}$ and $\mathrm{ALD}_{L,10}$ spectra. At ∼15.1 μm (P_8), there is a wide peak that is more defined in the $\mathrm{ALD}_{S,0}$ spectrum than in the $\mathrm{ALD}_{M,0}$ and $\mathrm{ALD}_{L,10}$ spectra. Longer wavelengths show a large dip at ∼19 μm (D_9) and a large peak at ∼21.8 μm (P_{10}).

The spectrum of each sample changes rather significantly as the regolith porosity increases. P_1 disappears, and some features only appear when the regolith porosity is high, such as D_3 (∼10.55 μm) and D_{10} (∼22.11 μm). The most notable change is the 10 μm region (9–13 μm). In this wavelength region, P_1 and D_4 decrease in spectral contrast, while P_5 increases in spectral contrast as the regolith porosity increases. The 10 μm region transitions from an emissivity dip to a broad emissivity peak with increasing regolith porosity. At longer wavelengths, P_8 and D_9 decrease in spectral contrast. Conversely, the spectral contrast of D_7 increases, with the spectral contrast being greatest in the high-porosity, fine-particulate (0–20 μm particle size) spectra. At high regolith porosities ($\geqslant$60%), the spectra for all particle sizes are largely identical to one another (Figure 3). The average emissivity of each spectrum decreases as the regolith porosity increases, where the average emissivity decreases more with increasing particle size.

3.2. Spectral Analysis

3.2.1. Feature Identification

Here, we describe the methods we used to understand the effect of regolith porosity on Allende's spectral features. First, we selected peaks and dips (i.e., spectral features) that could be diagnostic of constituent minerals in Allende using an interactive data language feature-finding program created for and described in A. C. Martin et al. (2022). Next, we located and calculated band parameters of the spectral features in each spectrum. The feature finding and band parameter analysis programs are fully described in A. C. Martin et al. (2022), and we provide a summary below.

For each spectral feature, we defined the continuum such that its end points lie tangent to the edges of each feature. The program returns the wavelength and spectral contrast of each feature. Other parameters that were calculated are the emissivity (calculated from Kirchhoff's law), width, full width at half max (FWHM), and area of each feature, which are provided online on Zenodo (see Data Availability). To calculate the spectral contrast (*SC*), we used the equation from R. N. Clark & T. L. Roush (1984), modified for emissivity:

$$SC = (\varepsilon_{\max} - \varepsilon_{\mathrm{cont}})/\varepsilon_{\mathrm{cont}}, \tag{3}$$

where $\varepsilon_{\max}$ is the maximum emissivity of the feature and $\varepsilon_{\mathrm{cont}}$ is the emissivity of the continuum at the same wavelength. We did not calculate the spectral contrast and FWHM of features that are too shallow and found on slopes (such as D_5; see Figure 2). To calculate the band parameters for the dips, we converted the spectra back to reflectance (i.e., $R = 1-\varepsilon$) so that the emissivity minima appear as peaks in the program. The error of each parameter was calculated by creating 10,000 synthetic spectra for each sample, where each data point was randomly generated from a normal distribution with a width defined by the corresponding error bars, as was done in A. C. Martin et al. (2022).

3.2.2. Effect of Regolith Porosity

Regolith porosity has numerous effects on the Allende spectra. P_1 disappears when the regolith porosity is $\geqslant$30%, whereas spectral features like D_3 and D_{10} only appear when the regolith porosity is $\geqslant$30%. Regolith porosity also has the effect of changing the position of some features (Figure 4). Most features in the 8–12 μm region do not significantly shift wavelengths as the regolith porosity increases, with P_2 and P_5 being two exceptions. P_5 shifts to longer wavelengths by ∼0.30, ∼0.40, and ∼0.38 μm for the $\mathrm{ALD}_{S,30\text{–}90}$, $\mathrm{ALD}_{M,0\text{–}90}$, and $\mathrm{ALD}_{L,10\text{–}90}$ spectra, respectively. P_2 is described in more detail in Section 4.1.1. Longward of 12 μm, D_7, D_8, D_9, and P_{10} shift significantly with increasing regolith porosity. For the $\mathrm{ALD}_{S,0\text{–}90}$, $\mathrm{ALD}_{M,10\text{–}90}$, and $\mathrm{ALD}_{L,30\text{–}90}$ spectra, D_7 shifts to longer wavelengths by ∼0.70, ∼0.58, and ∼0.40 μm, respectively. Averaged across all particle sizes, D_8, D_9, and P_{10} shift to shorter wavelengths by ∼1.23, ∼1.37, and ∼1.68 μm, respectively, as the regolith porosity increases. The position of P_{10} may be influenced by a volume-scattering peak being introduced at high regolith porosities ($\geqslant$30%), which could be causing the position to shift. The introduction of this volume-scattering feature may also be affecting the position of D_9 in $\mathrm{ALD}_{S,0\text{–}90}$, as it abruptly changes position (by 1.44 μm) when transitioning from $\mathrm{ALD}_{S,50}$ to $\mathrm{ALD}_{S,60}$.

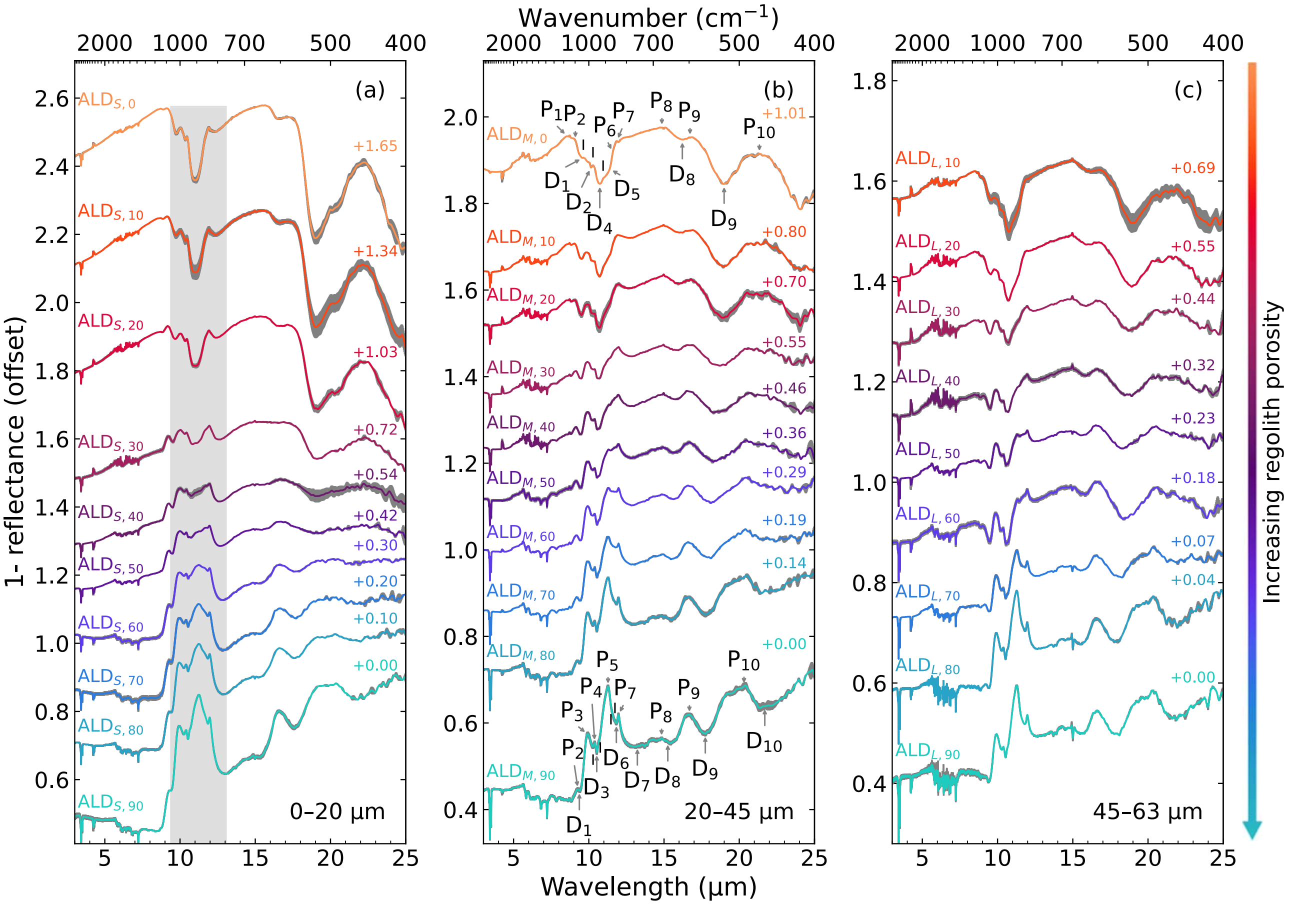

Figure 2. Offset reflectance spectra converted to emissivity of Allende with increasing regolith porosity (top to bottom). The vertical offset is labeled to the right for each spectrum. Standard deviations between multiple measurements are shaded in gray. Each panel shows the spectra for each particle size: (a) 0–20 μm (*S*), (b) 20–45 μm (*M*), and (c) 45–63 μm (*L*). The 10 μm region is shown within the gray box in (a). Panel (b) includes peaks labeled with P and dips labeled with D. Some features are marked with a black vertical bar for clarity. Note the different scales on the *y*-axes.

The spectral contrast of some peaks is also affected by the regolith porosity (Figure 5). Namely, the spectral contrast of P_3 increases nonlinearly from 3.2% to 13.7%, 0.3% to 14.7%, and from 1.1% to 13.2% for the $\mathrm{ALD}_{S,0\text{–}90}$, $\mathrm{ALD}_{M,0\text{–}90}$, and $\mathrm{ALD}_{L,10\text{–}90}$ spectra, respectively. The spectral contrast of P_5 also increases nonlinearly with increasing regolith porosity, and increases from 0.2% to 8.8%, 0.6% to 18.3%, and from 1.9% to 19.6% for the spectra of $\mathrm{ALD}_{S,30\text{–}90}$, $\mathrm{ALD}_{M,40\text{–}90}$, and $\mathrm{ALD}_{L,50\text{–}90}$, respectively. Conversely, the spectral contrasts of dips tend to decrease with increasing regolith porosity. For example, the spectral contrast of D_8 decreases from 24.8% to 6.7%, 28.1% to 6.5%, and from 20.3% to 7.2% for the $\mathrm{ALD}_{S,0\text{–}90}$, $\mathrm{ALD}_{M,0\text{–}90}$, and $\mathrm{ALD}_{L,10\text{–}90}$ spectra, respectively.

3.2.3. Effect of Particle Size

Particle size affects the spectral contrast of a few features. For example, the spectral contrast of D_7 (which we tentatively define as the TF) has a noticeable dependence on particle size at all regolith porosities, where the average spectral contrast is 71.3%, 26.0%, and 14.7% for the $\mathrm{ALD}_{S,0\text{–}90}$, $\mathrm{ALD}_{M,0\text{–}90}$, and $\mathrm{ALD}_{L,10\text{–}90}$ spectra, respectively. Additionally, particle size has an influence on the spectral contrast of the 10 μm region for the high regolith porosity spectra. The spectral contrast for the 10 μm feature for the spectra of $\mathrm{ALD}_{S,90}$, $\mathrm{ALD}_{M,90}$, and $\mathrm{ALD}_{L,90}$ is 43.7%, 39.0%, and 31.3%, respectively. In other words, the spectral contrast of the TF and the 10 μm region (when the regolith porosity is high) increases with decreasing particle size. Outside of spectral contrast, particle size does not have a significant effect on the parameters of most of the spectral features.

3.2.4. Low Regolith Porosity 0–20 μm Spectra

There are several features in the Allende spectra that behave oddly in $\mathrm{ALD}_{S,0\text{–}20}$, as several features are shifted to longer wavelengths than the features in $\mathrm{ALD}_{M,0\text{–}20}$ and $\mathrm{ALD}_{L,10\text{–}20}$. Specifically, P_1, P_3, P_8, P_9, P_{10}, D_1, D_2, D_4, and D_8 in $\mathrm{ALD}_{S,0\text{–}20}$ occur at longer wavelengths by ∼0.30 μm than features in $\mathrm{ALD}_{M,0\text{–}20}$ and $\mathrm{ALD}_{L,10\text{–}20}$. Interestingly, the positions of these features are similar for all spectra of samples with regolith porosities ⩾30%. For example, at a low regolith porosity of 10%, D_1 occurs at 9.687 μm in $\mathrm{ALD}_{S,10}$, and occurs at 9.524 and 9.539 μm in $\mathrm{ALD}_{M,10}$ and $\mathrm{ALD}_{L,10}$, respectively. At a higher regolith porosity of 40%, the positions are more similar, as D_1 occurs at 9.502, 9.457, and 9.505 μm in $\mathrm{ALD}_{S,40}$, $\mathrm{ALD}_{M,40}$, and $\mathrm{ALD}_{L,40}$, respectively.

Some spectral features—such as P_4, P_8, P_9, P_{10}, D_4, and D_9—have higher spectral contrasts in $\mathrm{ALD}_{S,0\text{–}20}$ than in $\mathrm{ALD}_{M,0\text{–}20}$ and $\mathrm{ALD}_{L,10\text{–}20}$. Yet, similar to the shifted spectral features described above, the difference in spectral contrast between spectral features in $\mathrm{ALD}_{S,0\text{–}20}$, and $\mathrm{ALD}_{M,0\text{–}20}$ and $\mathrm{ALD}_{L,10\text{–}20}$ is significantly smaller at regolith porosities ⩾30%. For example, D_9 has a spectral contrast of 182.9%,

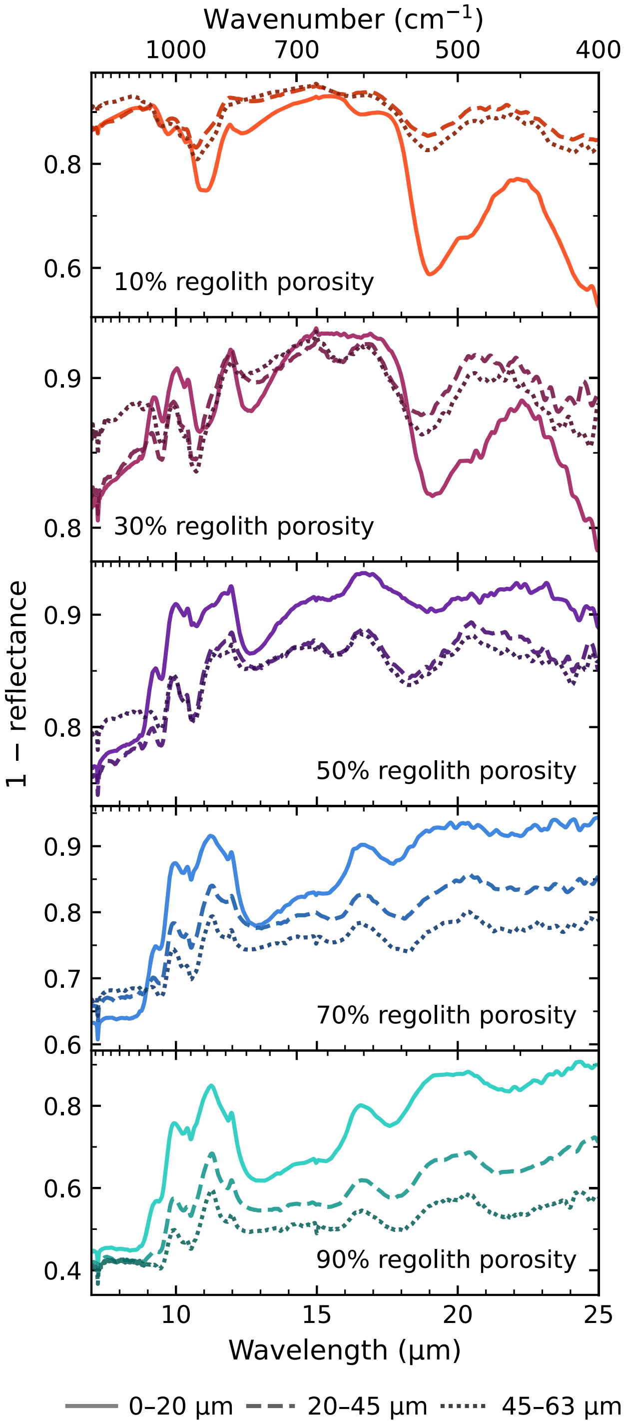

Figure 3. Comparison of Allende MIR spectra with different particle sizes. Solid lines represent 0–20 μm (*S*) spectra, dashed lines represent 20–45 μm (*M*) spectra, and dotted lines represent 45–63 μm (*L*) spectra.

84.6%, and 80.1% in $\mathrm{ALD}_{S,10}$, $\mathrm{ALD}_{M,10}$, and $\mathrm{ALD}_{L,10}$, respectively, whereas at a higher regolith porosity of 40%, the spectral contrast is 59.3%, 53.3%, and 51.0% in $\mathrm{ALD}_{S,40}$, $\mathrm{ALD}_{M,40}$, and $\mathrm{ALD}_{L,40}$, respectively.

4. Discussion

4.1. Comparisons to End-member Minerals

The results of our analysis of Allende's spectral features can be compared to end-member minerals studied by A. C. Martin et al. (2022, 2023), since their samples were prepared in the same way as described in Section 2.2. The end-member minerals we selected are olivine ($\mathrm{Mg}_{90.1}$; OLV_2 in A. C. Martin et al. 2022), enstatite ($\mathrm{Mg}_{89.7}$; ENS in A. C. Martin et al. 2023), and diopside ($\mathrm{Mg}_{92.8}$; DIOP_2 in A. C. Martin et al. 2023), as these minerals are similar to those found in the EMP analysis of Allende (see Section 2.1). Our goal here is to use the end-member mineral spectra to identify spectral features of Allende. For the Allende spectral features that correspond to an end-member mineral, we compared the band parameters to check for any variations as the regolith porosity is increased.

4.1.1. Spectral Feature Identifications

To identify spectral features in Allende, we first compared each Allende spectrum with each of the three end-member mineral spectra (i.e., OLV_2, ENS, and DIOP_2 from A. C. Martin et al. 2022, 2023) of the corresponding particle size and regolith porosity. Second, we qualitatively identified compositionally diagnostic features (e.g., RBs and volume-scattering features) in Allende spectra by comparing strong olivine and pyroxene end-member features to those we found in Allende. Lastly, we separately compared how the position and spectral contrast of each feature pair trends with increasing regolith porosity, and categorized each pair we matched into three tiers. We describe a feature pair as a "tier 1" match if the parameters of both features do not trend the same way with increasing regolith porosity (e.g., the spectral contrast increases for one feature, and decreases for the other). Feature pairs that are tier 1 matches are least likely to be caused by the same minerals, and matches are based entirely on similar spectral appearances and locations. A "tier 2" match is for pairs that have the same trend, but the trends have different shapes or slopes (e.g., one trends linearly and the other exponentially, but both overall trend positively), and are likely to be caused by the same minerals. A "tier 3" match is for features that trend the same way with increasing regolith porosity, their trends have the same shape, and are most likely to be caused by the same mineral. Figure 6 shows examples of features that meet the criteria to be categorized into each of the three tiers. Since each feature pair has three particle sizes, we assign a tier if at least two of three sizes meet the conditions of a tier. We also take into account the effect of Mg# and opaque minerals on the position and spectral contrast, respectively.

Since the Allende spectra strongly resemble the OLV_2 spectra and exhibit no definitive pyroxene features (Figure 7), we only identify olivine as major spectral features. Additionally, we have identified almost every Allende feature as an OLV_2 feature with varying tier matches for both position and spectral contrast. The Allende features that best match the OLV_2 features in the surface-scattering regime spectra (high regolith porosity) include D_1, D_4, D_8, and D_9, which we identify as olivine RBs. Likewise, P_4, P_5, P_7, and P_9 are olivine vibrational bands in volume-scattering regime spectra (high regolith porosity). Table 3 shows each Allende spectral feature and the corresponding feature from the OLV_2 spectra, along with the average position, average spectral contrast, and the match type for both the position and spectral contrast.

We assign the combination of P_1 (∼8.53 μm) and P_2 (∼9.17 μm) as the CF_1 in Allende because the position and shift in position with increasing regolith porosity of P_2 alone is consistent with olivine CFs, whereas both the width and the

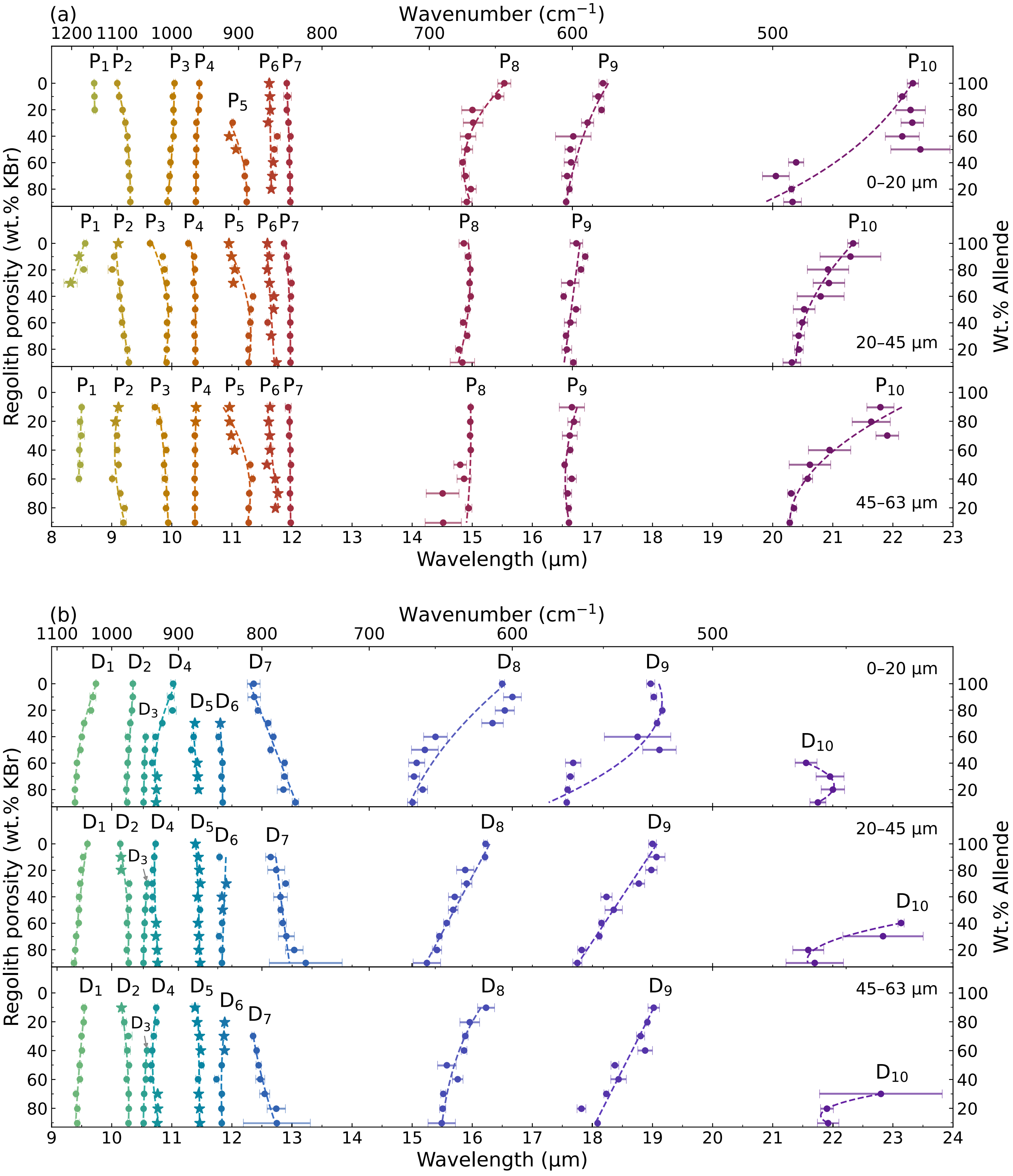

Figure 4. Positions of Allende features as a function of regolith porosity. Subplot (a) shows peaks (emissivity maxima), and subplot (b) shows dips (emissivity minima). Within each subplot, each panel from top to bottom shows the positions of the 0–20, 20–45, and 45–63 μm particle sizes. Points marked with stars represent shallow and sloped features.

decrease in spectral contrast with increasing regolith porosity of P_1 and P_2 combined is consistent with olivine CFs. P_2 shifts to longer wavelengths as regolith porosity increases, similar to the OLV_2 CF_1 (~8.99 μm) from A. C. Martin et al. (2022). P_2 shifts by ~0.22, ~0.28, and ~0.21 μm in $ALD_{S,0–90}$, $ALD_{M,0–90}$, and $ALD_{L,10–90}$, respectively. Similarly, the OLV_2 CF_1 shifts to longer wavelengths by ~0.34, ~0.35, and ~0.15 μm in $OLV_{2,S,0–70}$, $OLV_{2,M,0–90}$, and $OLV_{2,L,0–90}$. Though the Allende P_2 shifts a bit less, we attribute the difference to Allende having additional minerals mixed compared to the pure OLV_2 sample. This attribution is supported by the OLV_1 ($Mg_{91.0}$) CF_1, which contains minor phases of diopside, enstatite, spinel, and phyllosilicates, and shifts by a comparable amount to the Allende P_2. On average,

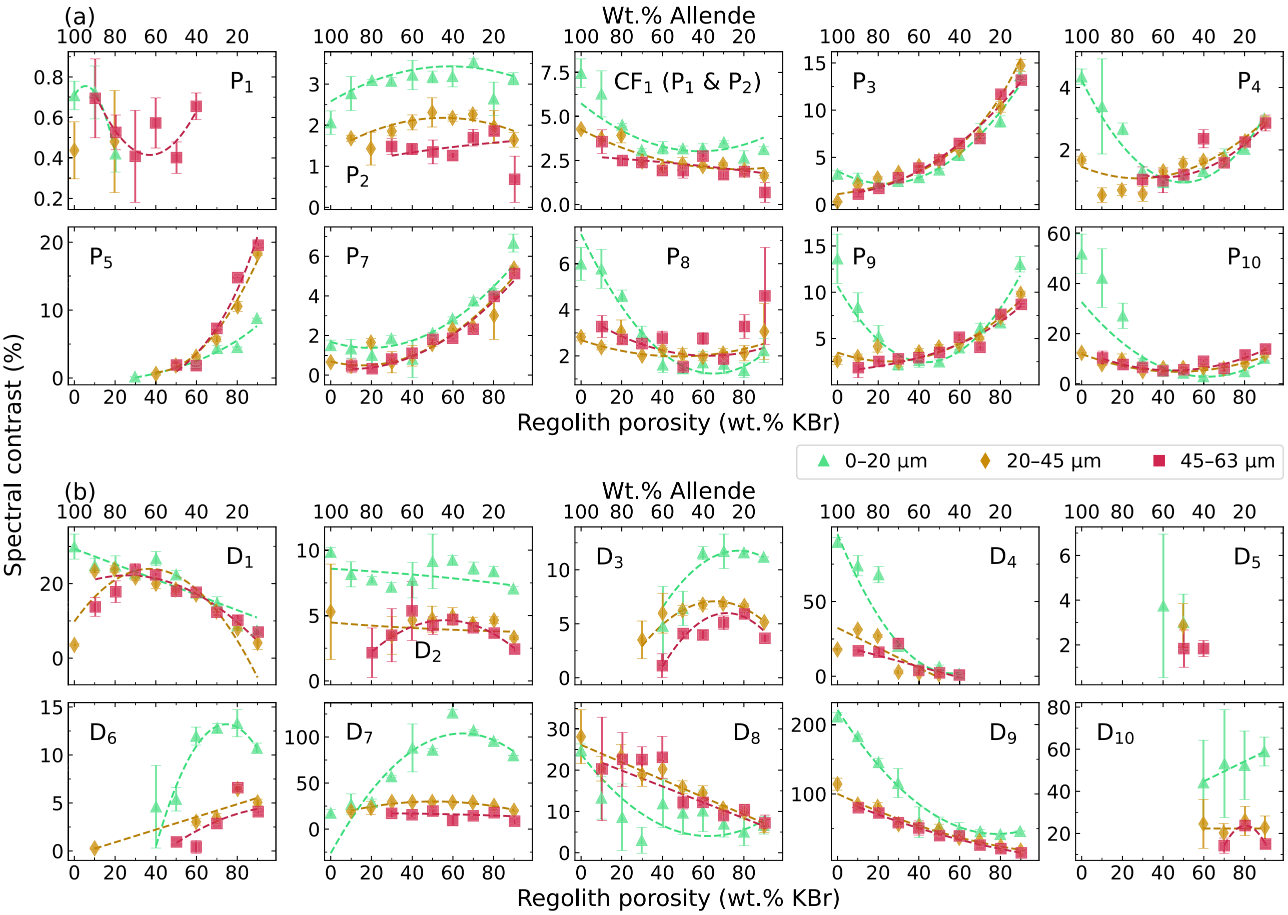

Figure 5. Spectral contrasts of defined Allende spectral features, calculated from Equation (3). Subplot (a) shows peaks (emissivity maxima), and subplot (b) shows dips (emissivity minima). In each subplot, green triangles denote spectral contrast values from the 0–20 μm spectra, yellow diamonds denote 20–45 μm spectra, and red squares denote 45–63 μm spectra.

the position of P_2 occurs at a longer wavelength than the OLV_2 CF_1 by ~0.20, ~0.14, and ~0.16 μm in the 0–20, 20–45, and 45–63 μm spectra, respectively, which we attribute to the Allende olivine being more fayalitic than OLV_2. Based on the evidence presented above, we rank the Allende P_2 and the OLV_2 CF_1 as a tier 3 match for position. The spectral contrast of the combined P_1 and P_2 decreases with increasing regolith porosity like the OLV_2 CF_1—which we also rank as a tier 3 match—whereas P_2 by itself does not (Figure 5). Additionally, the width of P_2 (~0.58 μm) is quite narrow compared to the width of the OLV_2 CF_1 (~1.49 μm; A. C. Martin et al. 2022). The combined feature width (P_1 and P_2) is ~1.80 μm. Furthermore, P_1 does not significantly shift positions like P_2 and the OLV_2 CF_1 (Figure 4), making the combination of P_1 and P_2 the best candidate for the Allende CF_1.

We identify P_8 (~14.93 μm) to be the CF_2 based on the feature's similarities to the CF_2 (~14.87 μm) identified in the OLV_2 spectra from A. C. Martin et al. (2022). Both spectral features shift to shorter wavelengths with increasing porosity; P_8 shifts by ~0.69, ~0.20, and ~0.47 μm in $\mathrm{ALD}_{S,0\text{–}90}$, $\mathrm{ALD}_{M,0\text{–}90}$, and $\mathrm{ALD}_{L,0\text{–}90}$, respectively, and the OLV_2 CF_2 shifts by ~0.44, ~0.54, and ~0.39 μm in $\mathrm{OLV}_{2,S,0\text{–}50}$, $\mathrm{OLV}_{2,M,0\text{–}70}$, and $\mathrm{OLV}_{2,L,0\text{–}90}$, respectively. We rank the pair as a tier 2 match for position due to the variations of how both features change across the three particle sizes. P_8 is also on average ~1.40 μm wider than the OLV_2 CF_2 (where the differences between the widths of both features are averaged over all particle sizes and regolith porosities where both features are present). As Allende is composed of a variety of olivines ($\mathrm{Mg}_{40\text{–}99}$), a wide CF_2 in the Allende spectra may be caused by a combination of olivine CF_2s with different Mg#s.

D_7 (~12.71 μm) is likely to be the TF, as both the position and spectral contrast match to the OLV_2 TF (~13.52 μm) with tier 3 matches (especially at high regolith porosities). Both features shift to longer wavelengths with increasing regolith porosity. D_7 shifts by ~0.70, ~0.58, and ~0.40 μm for the spectra of $\mathrm{ALD}_{S,0\text{–}90}$, $\mathrm{ALD}_{M,10\text{–}90}$, and $\mathrm{ALD}_{L,30\text{–}90}$, respectively, and the OLV_2 TF shifts by ~0.56, ~0.69, and ~2.58 μm for the $\mathrm{OLV}_{2,S,0\text{–}90}$, $\mathrm{OLV}_{2,M,0\text{–}90}$, and $\mathrm{OLV}_{2,L,0\text{–}90}$ spectra, respectively. The continuum of both features is defined from the peaks located at ~11.9 and ~16.6 μm (corresponding to the Allende P_7 and P_9, and the OLV_2 P_9 and P_{11}). At ⩾50% regolith porosity, the widths of D_7 and the OLV_2 TF are ~4.54 and ~4.55 μm, respectively. Interestingly, M. D. Lane et al. (2011) showed that the width of the TF in the spectra of <45 μm synthetic olivines increases with increasing Mg#. At lower regolith porosities (<50%), the widths of both features are hard to compare because the CF_2 (~14.9 μm) is sometimes defined as the long-wavelength end point of the continuum if its spectral contrast is high enough. The average spectral contrast across all regolith porosities of the TF in the OLV_2 spectra is 195.2%, 108.4%, and 65.0% for the $\mathrm{OLV}_{2,S,0\text{–}90}$, $\mathrm{OLV}_{2,M,0\text{–}90}$, and $\mathrm{OLV}_{2,L,0\text{–}90}$ spectra, respectively. Since the spectral contrast of the TF in the OLV_2 spectra shows a similar

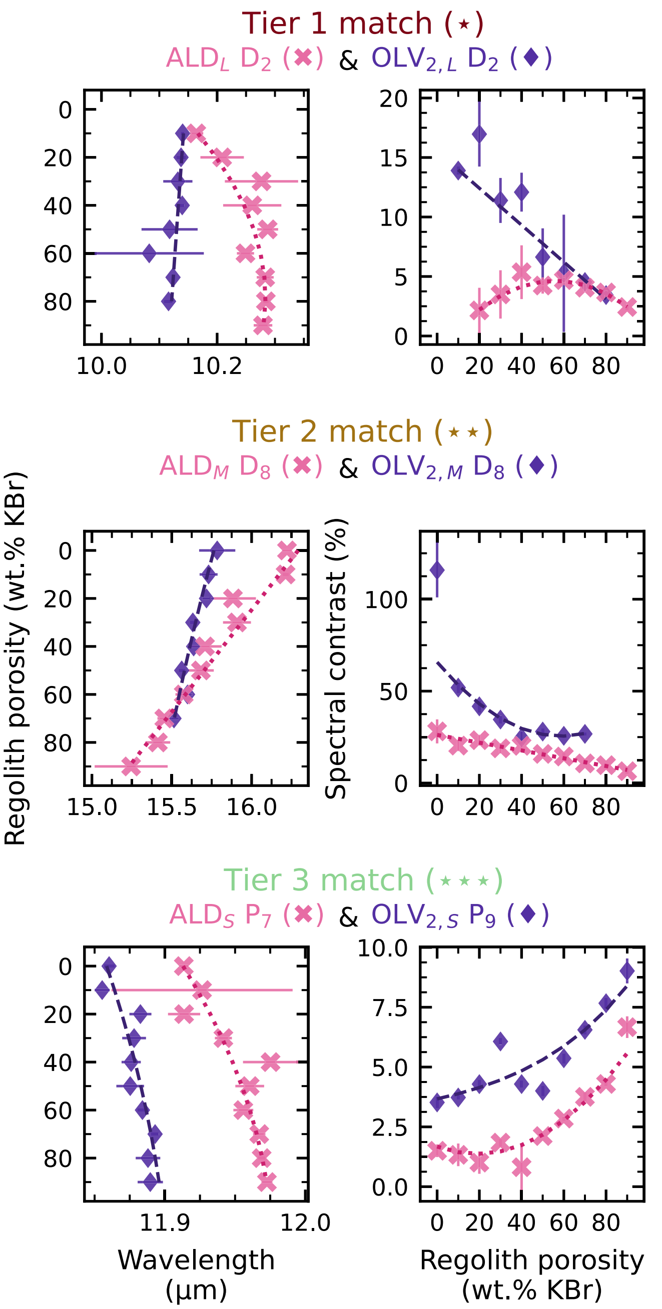

Figure 6. Positions and spectral contrasts of several Allende spectral features (pink crosses) and corresponding olivine features (purple diamonds). The top, middle, and bottom rows show examples of tier 1, 2, and 3 matches, respectively. The left column shows the change in position with increasing regolith porosity (regolith porosity vs. wavelength), and the right column shows the change in spectral contrast with increasing regolith porosity (spectral contrast vs. regolith porosity). A best-fit curve is shown to highlight the differences between how each feature changes with increasing regolith porosity, where the best-fit curve is dashed for the olivine features, and dotted for the Allende features.

dependence on particle size like D_7 (see Section 3.2.3), we identify the Allende D_7 as the TF.

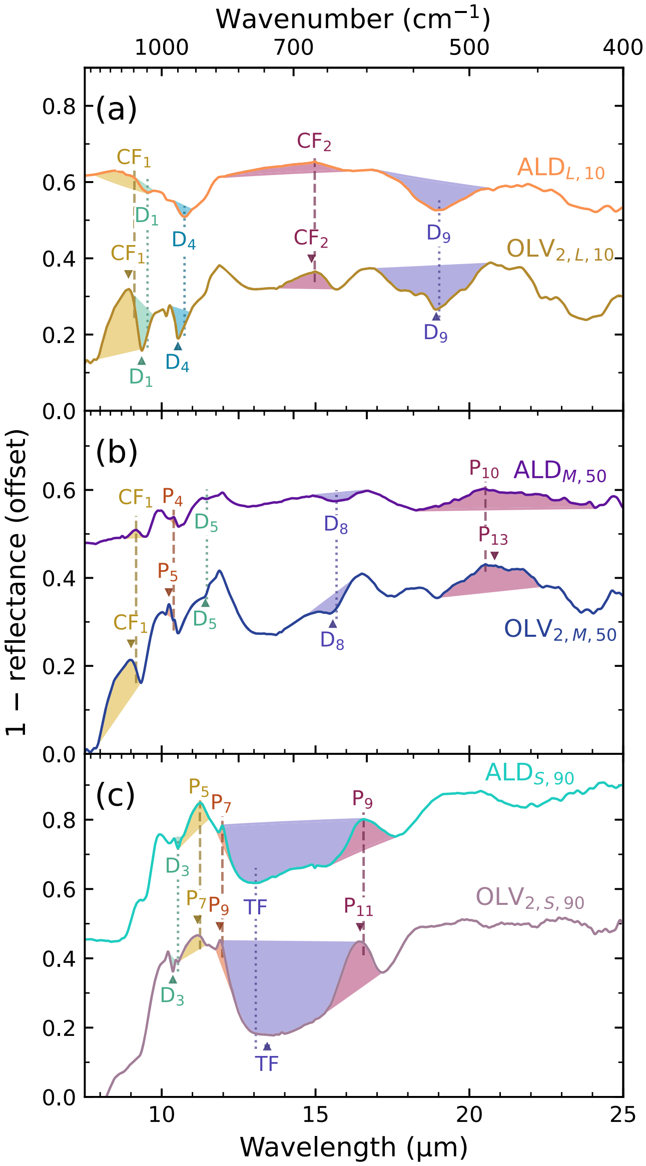

Figure 7. Each panel shows the spectrum of an Allende sample from this study and an olivine sample (OLV_2) from A. C. Martin et al. (2022). Panel (a) shows 45–63 μm (*L*) spectra with a regolith porosity of 10%, panel (b) shows 20–45 μm (*M*) spectra with a regolith porosity of 50%, and panel (c) shows 0–20 μm (*S*) spectra with a regolith porosity of 90%. Select features identified from both studies are labeled, with peaks labeled on top of each spectrum, and dips labeled on the bottom. Positions of Allende peaks and dips are marked with dashed and dotted lines, respectively, and positions of the corresponding OLV_2 features are marked with triangles. The area between each peak and its continuum is shaded. For the Allende spectra, we used the location of P_2 for the CF_1.

4.1.2. Effect of Opaque Minerals

In addition to silicates, Allende also contains opaque minerals (such as magnetite and carbonaceous material; e.g., H. Y. J. McSween 1977; C. M. O. D. Alexander et al. 2007). Opaques decrease the albedo and reduce the overall spectral contrast of MIR spectral features (e.g., C. L. Young et al. 2019; K. A. Shirley et al. 2023). We observed similar effects, where most of Allende's spectral features have lower spectral contrasts than their corresponding spectral features in the OLV_2 spectra (see Table 3 and Figure 7). For example, the spectral contrast of D_1 in the Allende spectra is less than the corresponding dip (D_1) in the OLV_2 spectra by ~26.9% for all regolith porosities and particle sizes. Similar to D_1, P_7 has a spectral contrast that is ~4.5% lower than its corresponding OLV_2 spectral feature (P_9). Conversely, P_5 has a higher spectral contrast than its corresponding OLV_2 spectral feature, P_7, by ~1.9%.

Table 3
Allende Features with Their Corresponding Features of the OLV_2 Spectra from A. C. Martin et al. (2022)

Feature Name		Average Position (μm)		Average Spectral Contrast (%)		Match Tier	
ALD	OLV_2	ALD	OLV_2	ALD	OLV_2	λ	SC
CF_1 (P_1 & P_2)[a]	CF_1 (P_2)	9.17 ± 0.02	8.99 ± 0.02	0.55 ± 0.29	19.59 ± 1.75	⋆⋆⋆	⋆⋆⋆
P_3	P_4	9.92 ± 0.02	9.98 ± 0.04	5.54 ± 0.30	1.63 ± 0.42	⋆⋆	n/a[b]
P_4	P_5	10.39 ± 0.01	10.23 ± 0.01	1.82 ± 0.22	6.94 ± 1.03	⋆⋆⋆	⋆⋆⋆
P_5	P_7	11.16 ± 0.02	11.03 ± 0.05	6.60 ± 0.21	4.72 ± 0.61	⋆⋆⋆	⋆⋆⋆
P_6	P_8	11.66 ± 0.03	11.59 ± 0.01	0.21 ± 0.11	0.57 ± 0.20	⋆	
P_7	P_9	11.96 ± 0.01	11.88 ± 0.01	2.17 ± 0.26	6.67 ± 0.49	⋆⋆⋆	⋆⋆⋆
CF_2 (P_8)	CF_2 (P_{10})	14.93 ± 0.09	14.87 ± 0.09	2.71 ± 0.41	3.91 ± 0.56	⋆⋆	⋆⋆
P_9	P_{11}	16.70 ± 0.08	16.57 ± 0.03	5.20 ± 0.55	11.56 ± 0.50	⋆⋆⋆	⋆⋆⋆
P_{10}	P_{13}	21.06 ± 0.20	22.24 ± 0.04	11.01 ± 1.67	17.86 ± 0.92	⋆	⋆⋆
D_1	D_1	9.49 ± 0.02	9.324 ± 0.01	17.07 ± 1.23	43.92 ± 2.39	⋆⋆⋆	⋆⋆
D_2	D_2	10.26 ± 0.02	10.12 ± 0.02	5.71 ± 0.87	9.44 ± 1.72	⋆	⋆
D_3	D_3	10.55 ± 0.01	10.37 ± 0.01	6.43 ± 0.81	11.20 ± 0.83	⋆⋆⋆	⋆⋆⋆
D_4	D_4	10.75 ± 0.02	10.54 ± 0.01	21.57 ± 1.82	26.93 ± 2.15	⋆⋆⋆	⋆⋆
D_5	D_5	11.44 ± 0.02	11.39 ± 0.05	2.66 ± 1.33	10.56 ± 11.10	⋆⋆	
D_6	D_6	11.83 ± 0.02	11.74 ± 0.03	5.75 ± 0.74	6.31 ± 3.99	⋆	
TF (D_7)	TF (D_7)	12.71 ± 0.11	13.52 ± 0.19	40.38 ± 3.36	109.36 ± 6.54	⋆⋆⋆	⋆⋆⋆
D_8	D_8	15.73 ± 0.11	15.63 ± 0.04	14.06 ± 3.46	25.89 ± 4.42	⋆⋆	⋆⋆
D_9	D_9	18.46 ± 0.09	18.20 ± 0.06	65.70 ± 5.46	73.82 ± 4.22	⋆⋆⋆	⋆⋆⋆

Notes. λ and SC denote the matched tier for the position and spectral contrast of each pair, respectively, where ⋆ = tier 1, ⋆⋆ = tier 2, and ⋆⋆⋆ = tier 3. For blank cells, there is not enough data to draw a conclusion.

[a] Here, we used P_2 for the average position. For the average spectral contrast, we used the combination of P_1 and P_2.

[b] The continua for these features are defined too differently, resulting in an unreliable comparison of spectral contrast.

While the presence of opaque material affects the spectral contrast of each feature in the Allende spectra differently, the appearance of each feature looks largely identical to the corresponding features in the pure olivine (OLV_2) spectra at all regolith porosities. Additionally, we have shown that the component minerals of a mixture can be identified by analyzing how the spectral features of the mixture spectrum change with increasing regolith porosity, and by comparing those changes to the corresponding spectral features of the minerals expected in the mixture. This result suggests that the effects of regolith porosity on MIR spectra are quantifiable even when darkening material is present, as is common on many low-albedo asteroids (e.g., A. S. Rivkin et al. 2019).

4.2. Spectral Features Indicative of Olivine and Porosity

4.2.1. Surface-scattering Regime

In the surface-scattering regime, the olivine spectral features that are traditionally the most indicative of composition are the CFs, RBs, and weak TFs (e.g., J. W. Salisbury et al. 1991; V. E. Hamilton 2000, 2010; M. D. Lane et al. 2011). Spectra of low regolith porosity Allende are indicative of being surface-scattering dominant based on the presence of CFs, high spectral contrast RBs, and a shallow TF. D_4, an olivine RB, is the best indicator of olivine composition when surface-scattering dominates in our Allende spectra. D4 is the deepest RB and, apart from $ALD_{S,0\text{–}20}$, the position of D_4 does not change significantly, making it a useful feature for assessing Mg#. As the regolith porosity increases, and spectra transition into the volume-scattering regime, the spectral contrast of D_4 decreases from 89.6% to 1.6%, 17.9% to 1.3%, and 17.0% to 0.9% in $ALD_{S,0\text{–}60}$, $ALD_{M,0\text{–}50}$, and $ALD_{L,10\text{–}60}$, respectively. By 60% regolith porosity, D_4 is too shallow to be used effectively for compositional identification. Additionally, the olivine RB D_9 may be used to identify olivine qualitatively, but it shifts to shorter wavelengths by ∼1.83, ∼1.31, and ∼0.97 μm for the $ALD_{S,0\text{–}90}$, $ALD_{M,0\text{–}90}$, and $ALD_{L,10\text{–}90}$ spectra, respectively, so it is not as accurate as D_4 for Mg# assessment.

Like D_4, the CF_1 (P_1 and P_2) may be useful for a qualitative identification of olivine at low regolith porosities. The P_1 portion of the CF_1 diminishes at 20%–30% regolith porosity (60% for the 45–63 μm spectra), making it unobservable in high regolith porosity spectra. Conversely, the P_2 portion of the CF_1 does not significantly change in spectral contrast for all particle sizes, but significantly shifts to longer wavelengths with increasing regolith porosity for the 0–20 and 20–45 μm spectra.

4.2.2. Volume-scattering Regime

Spectra that are dominated by volume-scattering display weak CFs and RBs, deep TFs, a broad 10 μm emissivity plateau, and peaks with high spectral contrasts (e.g., G. R. Hunt & L. M. Logan 1972; J. F. Mustard & J. E. Hays 1997; C. L. Young et al. 2019; A. C. Martin et al. 2023). As such, Allende spectra with regolith porosities ⩾50% are indicative of being volume-scattering dominant (Figure 2). We note that, since the low regolith porosity Allende spectra may not be entirely in the surface-scattering regime because particle sizes are relatively small (<63 μm), some volume-scattering features may be present even at low regolith porosities.

P_3 is well defined in all the Allende spectra, even in the low regolith porosity spectra (except for $ALD_{M,0}$). Since the spectral contrast of P_3 is highest in the $ALD_{S,90}$, $ALD_{M,90}$, and $ALD_{L,90}$ spectra (Figure 5), this feature stands out particularly well at high regolith porosities. As P_3 is likely an olivine spectral feature, its presence may be an indication of olivine, where the higher the spectral contrast, the higher the regolith porosity. However, P_3 does shift wavelengths by ∼0.16 μm with increasing regolith porosity, so it may not be a useful indication of olivine Mg#. As other minerals such as diopsides and phyllosilicates also have a spectral feature at ∼10 μm (e.g., M. M. McAdam et al. 2015; A. C. Martin et al. 2023), the presence of P_3 alone is not a definitive indicator of olivine.

One spectral feature that is a good indicator of both mineral composition and regolith porosity is P_5. When the regolith porosity is low (<50%), P_5 appears on a slope and is difficult to observe. However, the feature becomes more pronounced with increasing regolith porosity. Starting with a regolith porosity of ∼50%, the spectral contrast of P_5 increases nonlinearly for all particle sizes. Since we identified P_5 as an olivine feature (see Section 4.1.1), the presence of a strong ∼11.3 μm peak in a regolith could suggest abundant olivine and high regolith porosity. Of note, P_5 shifts ∼0.35 μm to longer wavelengths, so it may not be a good olivine Mg# indicator.

Like P_3, P_7 is an olivine spectral feature that is well defined in most of the Allende spectra (except $\mathrm{ALD}_{M,0}$, $\mathrm{ALD}_{L,10}$, and $\mathrm{ALD}_{L,20}$), and its spectral contrast is highest in the $\mathrm{ALD}_{S,90}$, $\mathrm{ALD}_{M,90}$, and $\mathrm{ALD}_{L,90}$ spectra. Because P_7 does not shift wavelengths considerably with regolith porosity, it is a good feature for assessing the Mg# of olivine. The presence of all the features described above (i.e., P_3, P_5, and P_7) in an MIR spectrum may be indicative of a surface containing olivine and a high surface porosity.

With the exception of P_3, the results above are consistent with those found by A. C. Martin et al. (2022) in that the OLV_2 P_7 is a useful indicator of an object with a high regolith porosity, and the OLV_2 P_9 is a useful indicator of olivine Mg# at high regolith porosities. Even though Allende contains darkening material, both the OLV_2 P_7 and OLV_2 P_9 match to Allende features with tier 3 matches for position and spectral contrast (Table 3), which reaffirms the utility of these two olivine features even when opaques are present.

4.3. Applications to Airless Bodies

4.3.1. Considerations for Analog Environment and Samples

There are several important differences between the spectra in our simulation and asteroid spectra measured from spacecraft that must be noted. Our reflectance spectra are measured under ambient Earth conditions, whereas asteroid regoliths are in a vacuum and have a thermal gradient within the upper hundred microns from their surfaces. Studies show that, when comparing the spectra of samples measured in a simulated asteroid environment (SAE) to spectra measured in ambient emissivity, the thermal and environmental differences can cause some spectral features—including CFs, RBs, and TFs—to shift positions and change in spectral contrast for low regolith porosity (0%) spectra (e.g., K. L. Donaldson Hanna et al. 2012, 2019; K. A. Shirley & T. D. Glotch 2019; M. S. Bramble et al. 2021a, 2021b).

For example, K. L. Donaldson Hanna et al. (2021) found that the CF_2 in the spectrum of Allende (0–105 μm particle size distribution) shifts to shorter wavelengths by ∼0.21 μm in the SAE spectrum compared to the ambient emissivity spectrum. Similarly, the position offset (i.e., the difference in position of a feature in an SAE spectrum compared to ambient emissivity) of the CF_1 in terrestrial olivine spectra with various particle sizes <125 μm could range from 0.11–0.31 μm (e.g., K. A. Shirley & T. D. Glotch 2019; M. S. Bramble et al. 2021b; K. L. Donaldson Hanna et al. 2021; A. C. Martin et al. 2025). However, the CF_1 in the Allende spectra do not have significant position offsets (<0.02 μm; K. L. Donaldson Hanna et al. 2019, 2021). The discrepancy between the position offset of the CF_1 in the olivine and Allende spectra may be due to Allende having a lower albedo than terrestrial olivine, which reduces the thermal gradient and thus reduces the effects of SAE conditions (e.g., J. W. Salisbury et al. 1991; K. L. Donaldson Hanna et al. 2019; M. S. Bramble et al. 2021a; K. L. Donaldson Hanna et al. 2021).

RB positions are not as affected by environmental conditions as CFs are (e.g., K. L. Donaldson Hanna et al. 2012; K. A. Shirley & T. D. Glotch 2019; M. S. Bramble et al. 2021b). Most notably, the olivine RB corresponding to D_4 has a position offset of 0–0.11 μm when comparing SAE spectra to ambient emissivity spectra (K. L. Donaldson Hanna et al. 2021; A. C. Martin et al. 2025) and ∼0.15 μm when comparing SAE spectra to ambient reflectance spectra (A. C. Martin et al. 2025), making D_4 a particularly useful indicator of olivine at low regolith porosities. While the environmental effects described above mostly pertain to SAE spectra compared to ambient emissivity spectra, the feature positions of ambient emissivity and reflectance spectra of the same sample are largely similar (e.g., J. W. Salisbury et al. 1991; M. D. Lane et al. 2011; A. C. Martin et al. 2025). We take the above environmental effects into account when comparing our ambient laboratory spectra to asteroid emissivity spectra (Section 4.3.2).

KBr is commonly used in MIR studies to simulate regolith porosity because it's MIR-transparent (e.g., P. Vernazza et al. 2012; C. L. Young et al. 2019; M. R. M. Izawa et al. 2021; A. C. Martin et al. 2022, 2023). The spectrum of silicates embedded in pressed KBr pellets can result in minor feature position offsets and slight modifications of feature shape due to photons passing directly from KBr ($n = 1.53$) into the silicate grain (A. Tamanai et al. 2006). However, as our samples are loose powders, the KBr contacts a small fraction of the grain's surface area, and we have therefore effectively avoided this problem. Future studies using other MIR-transparent salts with different real refractive indices could be implemented to calibrate the potential minor contributions from the use of KBr.

4.3.2. Comparisons to Asteroid Spectra

Here, we compare our Allende spectra to MIR emissivity spectra of four asteroids observed by the Spitzer Space Telescope (SST; M. W. Werner et al. 2004): (85989) 1999 JD_6 (L-type), (114) Kassandra (K-type), (5261) Eureka (Sa-type), and (234) Barbara (L-type). K- and L-type asteroids are of particular interest because these asteroids have previously been linked to CV chondrites using VNIR spectroscopy (e.g., J. F. Bell 1988; R. P. Binzel et al. 2001; T. Mothé-Diniz et al. 2008; J. Eschrig et al. 2021; F. E. DeMeo et al. 2022; M. Mahlke et al. 2023), and L-type asteroids and Allende both contain abundant CAIs (e.g., H. Y. J. McSween 1977; A. S. Kornacki & J. A. Wood 1984; J. M. Sunshine et al. 2008; M. Devogèle et al. 2018). We selected asteroids 1999 JD_6 and Kassandra for analysis here because their VNIR spectra from the Massachusetts Institute of Technology-Hawaii Near-Earth Object Spectroscopic (MITHNEOS[3]) survey are similar to VNIR Allende spectra measured from the Reflectance Experiment LABoratory (RELAB[4]), as determined by

---

[3] http://smass.mit.edu/minus.html

[4] https://sites.brown.edu/relab/

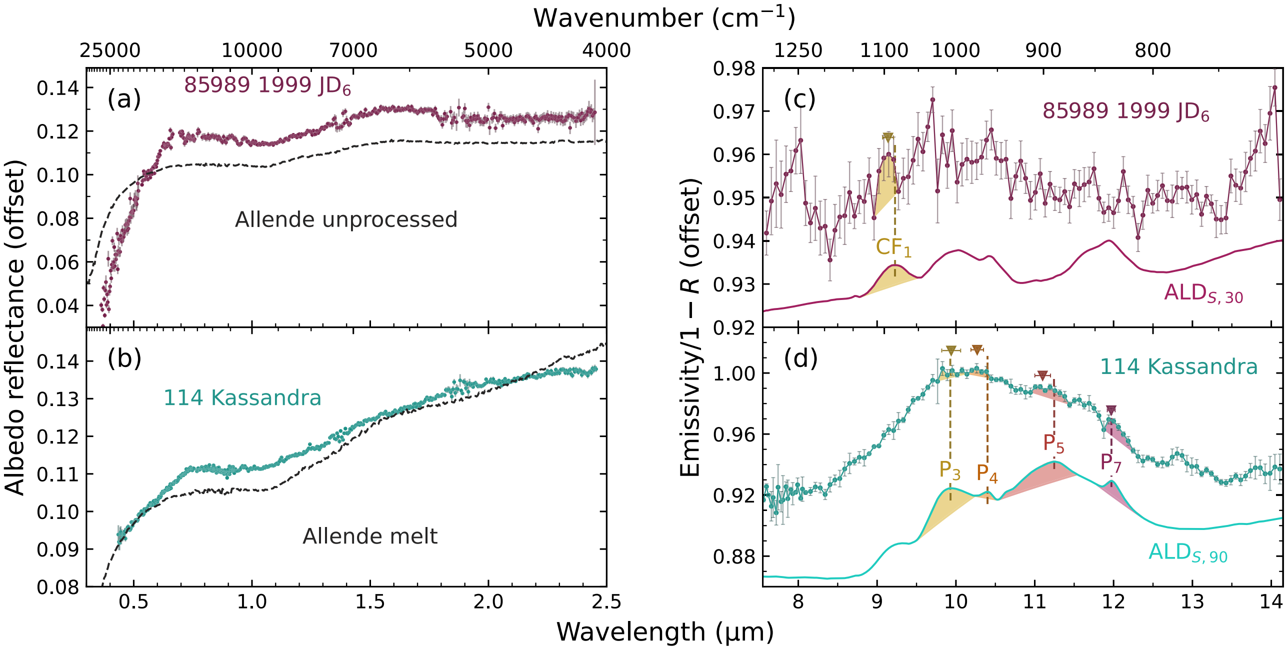

Figure 8. (a) The VNIR reflectance spectra of an Allende sample with a particle size of 0–75 μm from RELAB (MS-CMP-040-A; dashed gray line), and 1999 JD$_6$ (purple points) measured by MITHNEOS (R. P. Binzel et al. 2019). The spectrum of 1999 JD$_6$ is scaled by 0.15 based on the geometric albedo (J. de León et al. 2010). (b) The VNIR spectra of a 0–75 μm Allende sample with melted/fused grains from RELAB (MS-CMP-040-C; dashed gray line), and the asteroid 114 Kassandra (dark cyan points) measured by SpeX (J. T. Rayner et al. 2003; F. E. DeMeo et al. 2009). Kassandra is scaled by 0.0884 based on the albedo measurement from E. Dotto et al. (2002). All VNIR spectra are normalized to a reflectance of 0.10 at 0.55 μm. (c) The MIR emissivity spectrum of 1999 JD$_6$ measured by the SST (dark purple solid line with points), and ALD$_{S,30}$ (light purple solid line) scaled by 0.18 and offset for comparison. (d) The MIR spectra of Kassandra (dark cyan solid line with points) and ALD$_{S,90}$ (cyan solid line), which is scaled by 0.19 and offset. The full 5.12–14.11 μm spectrum of Kassandra is in Figure A1. For (c) and (d), several Allende peaks are located using dashed vertical lines and are compared to possible corresponding peaks in their respective asteroid spectrum (marked by triangles). The area between each peak and its continuum is shaded.

D. Kuroda et al. (2021) and F. E. DeMeo et al. (2009), respectively. Asteroids Eureka and Barbara were selected because they are compositionally similar to Allende (e.g., A. S. Rivkin et al. 2007; D. E. Trilling et al. 2007; J. M. Sunshine et al. 2008; M. Devogèle et al. 2018). We note that we only compare spectral features of the SST asteroids that may correspond to Allende features—we do not perform a detailed compositional analysis of the asteroids. The SST spectral reduction is detailed in the Appendix.

Each MIR Allende spectrum was scaled to have the same emissivity range as the asteroid spectrum (excluding outliers) it was being compared with, to control for albedo and particle size effects. Additionally, we again note that the Allende spectra reported here were taken under ambient conditions, and MIR spectra are sensitive to the conditions in which they are taken (e.g., K. L. Donaldson Hanna et al. 2017; see Section 4.3.1). After each Allende spectrum was scaled, we vertically shifted them so that the average emissivity was the same as the average emissivity of the asteroid. The resolution of each Allende spectrum was then reduced to match the resolution of the asteroid spectra. We then performed an rms error analysis to determine the best-matching Allende spectrum for each asteroid spectrum, a technique that has been used previously (e.g., M. S. Ramsey & P. R. Christensen 1998; V. C. Lowry et al. 2022) and is given by

$$\sqrt{\sum_{j=1}^{m}\frac{\delta(\lambda)_j^2}{m}}, \tag{4}$$

where m is the number of wavelengths and $\delta(\lambda)$ is the difference in emissivity between the asteroid and the Allende spectra (i.e., the residual error) at each wavelength. The Allende spectrum with the lowest rms error is considered the closest match for a given asteroid.

Asteroid 1999 JD$_6$ is a contact binary near-Earth asteroid (NEA), and was classified as an L-type by R. P. Binzel et al. (2019). As noted by D. Kuroda et al. (2021), the near-infrared (NIR; 0.8–2.5 μm) spectrum of 1999 JD$_6$ is similar to the NIR spectrum of Allende, but the visible (0.3–0.8 μm) portion of the two spectra do not match as well (Figure 8(a)). Kassandra is a main belt asteroid that was classified as an Xk-type by S. J. Bus & R. P. Binzel (2002) and later as a K-type by F. E. DeMeo et al. (2009). The VNIR spectrum of Kassandra is similar to the VNIR spectrum of a 0–75 μm Allende sample with melted/fused grains (Figure 8(b)). We note that, although the VNIR spectra of the unprocessed (Figure 8(a)) and the melted (Figure 8(b)) Allende samples from RELAB have different spectral slopes, the MIR spectra of the same two samples are mostly identical.

In Figure 8(c), we compare the MIR spectrum of 1999 JD$_6$ to ALD$_{S,30}$, as it is the closest matching Allende spectrum based on Equation (4). Unlike the NIR spectra, the MIR spectra of 1999 JD$_6$ does not closely resemble ALD$_{S,30}$. The only spectral feature that these two spectra may share is a peak at 9.12 ± 0.09 μm in 1999 JD$_6$'s spectrum, which may correspond to the CF$_1$ (P$_2$; ~9.23 μm) in ALD$_{S,30}$. Both features are positively sloped, but P$_2$ is wider and its slope is less steep. The 1999 JD$_6$ spectrum may share more features with ALD$_{S,30}$, but the low SNR precludes more detailed comparison. The differences in spectral features may be due to differences in composition. Additionally, the absence of P$_5$ and the presence of a CF$_1$ in the spectrum of 1999 JD$_6$ suggest that

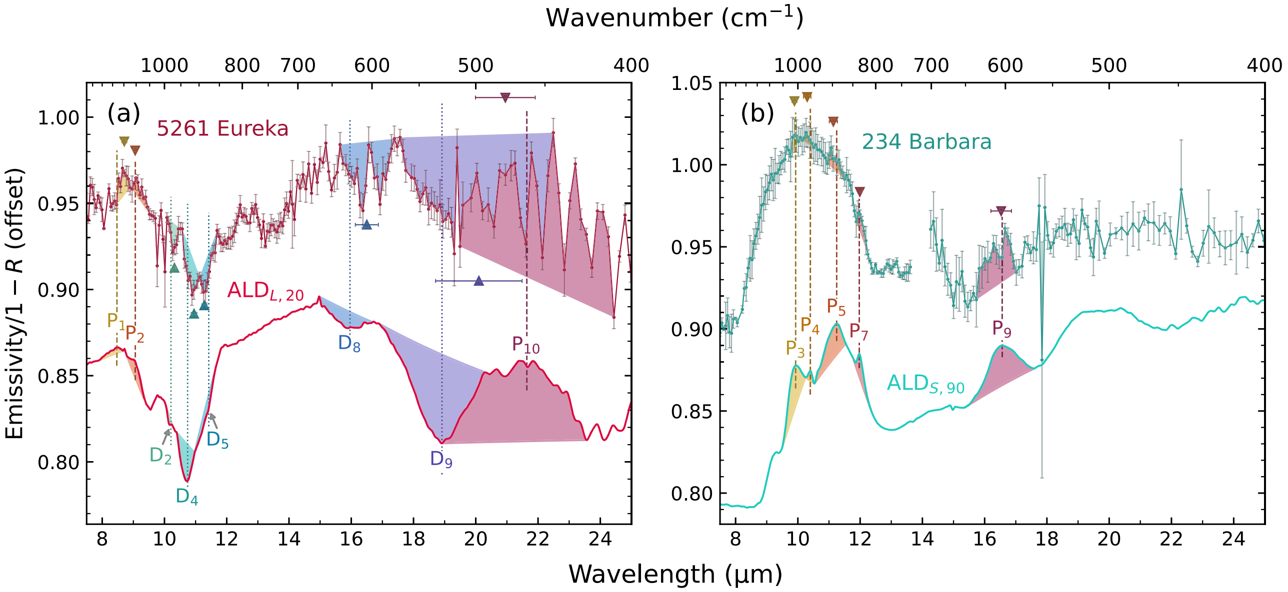

Figure 9. (a) MIR emissivity spectrum of Eureka measured by the SST (dark red solid line with points), and ALD$_{L,20}$ (red solid line) scaled by 0.79 and offset for comparison. (b) MIR spectra of Barbara (dark cyan solid line with points) and ALD$_{S,90}$ (cyan solid line), which is scaled by 0.28 and offset. In the spectrum of Barbara, the 13.65–14.15 μm region is removed because the SST has an artifact at those wavelengths, which is documented in Section 7.3.8 in the Infrared Spectrograph Instrument Handbook (https://irsa.ipac.caltech.edu/data/SPITZER/docs/irs/irsinstrumenthandbook/). For both (a) and (b), several Allende peaks and dips are located using dashed and dotted vertical lines, respectively, and are compared to possible corresponding features in their respective asteroid spectrum (marked by triangles). The area between each feature and its continuum is shaded. Figure A1 shows the full 5.2–38 μm spectra of both Eureka and Barbara.

Table 4

Positions (in μm) of Allende Features Corresponding to SST Asteroid Spectra

	ALD$_{S,90}$ and Kassandra			ALD$_{L,20}$ and Eureka			ALD$_{S,90}$ and Barbara	
P$_3$	9.93 ± 0.01	9.94 ± 0.12	P$_1$	8.47 ± 0.04	8.71 ± 0.08	P$_3$	9.93 ± 0.01	9.89 ± 0.08
P$_4$	10.40 ± 0.01	10.27 ± 0.08	P$_2$	9.06 ± 0.01	9.07 ± 0.07	P$_4$	10.40 ± 0.01	10.30 ± 0.12
P$_5$	11.25 ± 0.01	11.09 ± 0.10	P$_{10}$	21.64 ± 0.32	21.75 ± 1.15	P$_5$	11.25 ± 0.01	11.14 ± 0.13
P$_7$	11.97 ± 0.01	11.97 ± 0.05	D$_2$	10.21 ± 0.04	10.31 ± 0.07	P$_7$	11.97 ± 0.01	11.99 ± 0.06
			D$_4$	10.74 ± 0.02	10.94 ± 0.10	P$_9$	16.56 ± 0.1	16.53 ± 0.33
			D$_5$	11.42 ± 0.02	11.28 ± 0.08			
			D$_8$	15.96 ± 0.16	16.42 ± 0.36			
			D$_9$	18.98 ± 0.10	19.53 ± 0.94			

the surface of 1999 JD$_6$ might have a low regolith porosity. For the total porosity (Φ) of 1999 JD$_6$ (i.e., the percentage of empty space within a given volume, as determined by Equation (2) and given in Table 2), we note that the total porosity of ALD$_{S,30}$ is $\Phi = 77.77\%$, so we expect 1999 JD$_6$ to have a similar value such as $\Phi \sim 80\%$, although the two spectra do not resemble each other well enough to make this a precise estimation.

The MIR spectrum of Kassandra best resembles ALD$_{S,90}$ (Figure 8(d)). Similar spectral features between the two MIR spectra are P$_3$, P$_4$, P$_5$, and P$_7$ (Table 4). The most notable spectral features in Kassandra's spectrum are at 10.27 and 11.97 μm (corresponding to P$_4$ and P$_7$, respectively). The 10.27 μm Kassandra peak has a similar shape to P$_4$, but occurs at a slightly shorter wavelength. Similarly, the shape of the 11.97 μm peak resembles P$_7$, and both peaks occur at about the same position. Since P$_4$ and P$_7$ are tier 3 matches to OLV$_2$ features for both position and spectral contrast, the corresponding Kassandra spectral features could also be due to olivine. However, there are quite a few differences between the two spectra. P$_3$ and P$_4$ in ALD$_{S,90}$ have relatively lower emissivity values compared to P$_5$, whereas in the Kassandra spectrum, the 9.9 and 10.27 μm peaks (corresponding to P$_3$ and P$_4$, respectively) have higher emissivity values than the 11.1 μm peak (corresponding to P$_5$). The peak position of the whole 10 μm feature in ALD$_{S,90}$ is also slightly longward of the 10 μm feature in the Kassandra spectrum. The differences between the two spectra suggest that Kassandra and Allende are not completely composed of the same minerals. E. Dotto et al. (2002) noted that the MIR spectrum of Kassandra (observed by the Infrared Space Observatory from 2.5 to 11.6 μm; M. F. Kessler et al. 1996) displays a CF$_1$ at ~9.2 μm, similar to the Ornans meteorite. However, the spectrum of Kassandra from the SST presented here does not show a strong CF$_1$ at the same wavelength. The absence of a prominent CF$_1$ and the presence of P$_5$ in Kassandra's MIR spectrum is an indicator that Kassandra's regolith is highly porous ($\Phi \gtrsim 90\%$).

Eureka is an Sa-type Mars Trojan asteroid that is rich in olivine (e.g., A. S. Rivkin et al. 2007; D. E. Trilling et al. 2007; F. E. DeMeo et al. 2009). The spectrum for Eureka is best matched by ALD$_{L,20}$ (Figure 9(a)) as the two spectra share many spectral features: P$_1$, P$_2$, P$_{10}$, D$_2$, D$_4$, D$_5$, D$_8$, and D$_9$ (Table 4). Like the Allende CF$_1$ (P$_1$ and P$_2$), Eureka has a similar pair of peaks at 8.71 and 9.07 μm. Feature pairs that are most similar to each other (based on position and continuum slope) are the 9.07, 10.31, and 10.9 μm features in Eureka's spectrum (corresponding to P_2, D_2, and D_4, respectively). The 9.07 μm peak could be an olivine CF_1 due to its resemblance to P_2, and the 10.9 μm dip is likely an olivine RB based on its similarities to D_4. The presence of P_2 (CF_1) and D_4 in Eureka's spectrum strongly suggests that Eureka has a low total porosity. Since the features of Eureka's spectrum occur at slightly longer wavelengths than most of the corresponding Allende features noted in Table 4, we suggest that the olivine Mg# on the surface of Eureka is on the lower end of the Allende Mg# range ($Mg_{40–99}$), which is consistent with the composition of Mg_{49} for Eureka reported by J. A. Sanchez et al. (2014). Eureka's MIR spectrum is similar to R chondrites, brachinites, and chassignites, which contain 65–93 vol% olivine ($Mg_{60–70}$; L. F. Lim et al. 2011b and references therein). In comparison, Allende contains 82.7–83.9 vol% olivine (excluding large inclusions; P. A. Bland et al. 2004; K. T. Howard et al. 2010), and a wider variety of olivine compositions ($Mg_{40–99}$). Lastly, we suggest Eureka has a total porosity of $\Phi \sim 70\%$ based on the total porosity of $ALD_{L,20}$ ($\Phi = 68.35\%$; Table 2).

Barbara is an L-type asteroid located in the main asteroid belt (e.g., J. M. Sunshine et al. 2008; F. E. DeMeo et al. 2009). We compare the MIR spectrum of Barbara to the best-matching Allende spectrum, $ALD_{S,90}$, in Figure 9(b). The spectrum of Barbara displays a broad 10 μm emissivity plateau similar to the Allende samples with high regolith porosities ($\geqslant 60\%$). Similar spectral features between the two spectra include P_3, P_4, P_5, P_7, and P_9 (Table 4). Of these, the peaks located at 10.3, 11.99, and 16.5 μm in Barbara's spectrum are most similar to their corresponding Allende peaks (P_4, P_7, and P_7, respectively). Similar to Kassandra, P_3 and P_4 have lower emissivity values compared to P_5, but the 9.89 and 10.3 μm peaks (corresponding to P_3 and P_4) have higher emissivity values than the 11.1 μm peak (corresponding to P_5) in the Barbara spectrum. The surface of Barbara is primarily composed of olivine with 20–25 vol% of CAIs (J. M. Sunshine et al. 2008; M. Devogèle et al. 2018). Allende is also primarily composed of olivine, but contains 2.2–9.4 vol% of CAIs (H. Y. J. McSween 1977; A. S. Kornacki & J. A. Wood 1984), which could mean that differences between the two spectra are due to the different abundances of the CAIs. As with Kassandra, the presence of P_5 and the overall shape of the 10 μm emissivity plateau in the spectrum of Barbara suggests that Barbara's surface may have a high total porosity ($\Phi \gtrsim 90\%$).

5. Conclusion

Regolith porosity and particle size are both important properties to consider when interpreting the MIR spectra of asteroids. To aid in such interpretation, we have analyzed the MIR spectra of three particle sizes of the Allende CV 3 chondrite mixed with KBr to simulate regolith porosity. Our results suggest that (1) particle size primarily affects the spectral contrast of some features. Most notably, the 10 μm region (when the regolith porosity is high) and the TF (at all regolith porosities) both show an increase in spectral contrast as particle size decreases. (2) Regolith porosity significantly alters the spectra by shifting the positions of some spectral features and by altering the spectral contrast of features. Points (1) and (2) are consistent with previous studies of the spectral effects of the regolith porosity (e.g., A. C. Martin et al. 2022, 2023). (3) The Allende spectra presented here are very similar to the pure olivine spectra presented by A. C. Martin et al. (2022), but overall, features have lower spectral contrasts and slight variations. We did not observe any significant contributions due to pyroxene features in our Allende spectra. Since Allende is a meteorite with mixtures of minerals and opaques, its similarities to the olivine spectra show that the effects of regolith porosity may be measured regardless of albedo (important because many asteroids have low albedos), and that olivine is spectrally dominant in the MIR.

Comparing the Allende spectra to asteroids' allows for their total porosities and surface compositions to be constrained. Asteroids 1999 JD_6 and Eureka likely have low total porosities ($\Phi \sim 80\%$ and $\Phi \sim 70\%$, respectively), while Kassandra and Barbara likely have high total regolith porosities ($\Phi \gtrsim 90\%$). Eureka shows strong spectral evidence of Olivine in the MIR and is overall more fayalitic than Allende, Kassandra and Barbara show some spectral signatures of olivine, and 1999 JD_6 shows little evidence of olivine. While none of the Allende spectra provide a perfect match to the asteroids used in this study, this work shows how laboratory MIR spectral measurements may be used to better constrain the composition and regolith porosity of all asteroids, including meteorite parent bodies.

Acknowledgments

The authors would like to thank the two anonymous referees for their reviews, which improved the quality of this article. We also thank Mark Loeffler for access to the FTIR spectrometer, and Molly McCanta and Allan Patchen for the EMP data acquisition. Part of the data utilized in this publication were obtained and made available by the MITHNEOS Survey. The Infrared Telescope Facility is operated by the University of Hawaii under contract 80HQTR19D0030 with NASA. The MIT component of this work is supported by NASA grant 80NSSC18K0849. This research utilizes spectra acquired by Carle M. Pieters (MS-CMP-040-A/cams40 and MS-CMP-040-C/ccms40) with the NASA RELAB facility at Brown University. This work was based (in part) on observations made with the Spitzer Space Telescope, which was operated by the Jet Propulsion Laboratory, California Institute of Technology, under contract with NASA.

This work is supported by NASA's Science Mission Directorate Research and Analysis Solar System Workings program NH19ZDA001N, as well as the Interns-2-Scholars program at Northern Arizona University. Any opinions, findings, and conclusions or recommendations expressed in this material are those of the authors and do not necessarily reflect the views of NASA or the National Science Foundation. Parts of the results in this work make use of the color maps in the CMasher package for Python (E. van der Velden 2020). We would also like to acknowledge that this work was primarily done in northern Arizona, at the base of the San Francisco Peaks, on homelands sacred to Native Americans throughout the region.

Data Availability

All data resulting from this paper are available on Zenodo under an open-source Creative Commons Attribution license: doi:10.5281/zenodo.12808383 (L. D. Dausend et al. 2024).

Appendix
SST Data Reductions and Thermal Modeling

Asteroids Kassandra, Barbara, Eureka, and 1999 JD$_6$ were observed with the infrared spectrograph (IRS; J. R. Houck et al. 2004) on the SST between 2004 and 2008. The IRS measures spectral flux in low resolution mode ($\lambda/\Delta\lambda \sim$64–128) from 5.2 to 38 μm in four segments: short wavelength, low resolution, second order (SL2; 5.2–8.5 μm); short wavelength, low resolution, first order (SL1; 7.4–14.2 μm); long wavelength, low resolution, second order (LL2; 14.0–21.5 μm); and long wavelength, low resolution, first order (LL1; 19.5–38.0 μm). Asteroid 1999 JD$_6$ was observed in SL1, Kassandra in SL2 and SL1, and both Barbara and Eureka were observed in all four segments. Circumstances of the observations are in Table A1. Kassandra was also observed in the high-resolution mode ($\lambda/\Delta\lambda \sim$600) from 9.9 to 37.2 μm, but we only present the flux from SL2 and SL1. The spectra of the asteroids were reduced using the methods described in J. P. Emery et al. (2006), which we will summarize here.

We began the data reduction by downloading the basic calibrated data files produced from Spitzer Science Center (SSC) on the Spitzer Heritage Archive[5] (pipeline version S18.18). The images are dark and flat corrected, and excess emission was subtracted by switching between two dithering positions. The target center is identified by fitting the spatial dimension with a Gaussian, which was then fit to a second-degree polynomial with outliers omitted. Next, we summed the flux within each extraction width appropriate for the point-spread function (PSF) at each wavelength. Since the SST is diffraction limited, the PSF is wavelength dependent. Therefore, we use extraction widths used by the SSC: $7''\!.2$, $14''\!.4$, $21''\!.68$, and $36''\!.58$ at 6, 12, 16, and 27 μm, respectively, which we varied linearly with wavelength across the signal. Each order is scaled based on regions where the wavelengths overlap for continuity, and lastly, the entire spectrum is scaled by the average of each order's scale factor.

To model the spectral energy distribution (SED) of our targets, we begin by noting that the SED in this wavelength region is dependent on the object's size, composition, and temperature distribution. By modeling the SED using the NEA Thermal Model (NEATM; A. W. Harris 1998), we derived estimates for the subsolar temperature (T_{SS}), beaming parameter (η), radius (R), and visible geometric albedo (p_v) for each asteroid (Table A2). The NEATM is a modification of the Standard Thermal Model (e.g., L. A. Lebofsky & J. R. Spencer 1989) and has been successfully applied to non-NEA objects in previous studies (e.g., J. P. Emery et al. 2006; L. F. Lim et al. 2011a; J. Licandro et al. 2012; A. Morlok et al. 2020; A. C. Martin & J. P. Emery 2023).

The NEATM assumes a spherical shape and radiative equilibrium at the asteroid's surface, which results in an expression for T_{SS}:

$$T_{SS} = \left[\frac{S_0(1 - A_B)}{r_{AU}^2 \sigma \varepsilon_{bol} \eta}\right]^{1/4}, \tag{A1}$$

where S_0 is the solar flux at 1 astronomical unit (au; 1374 W m^{-2}), A_B is the bolometric bond albedo, r is the Sun–asteroid distance in au (obtained from JPL Horizons[6] at the time of each observation), σ is the Stefan–Boltzmann constant (5.67×10^{-8} W m^{-2}), and $\varepsilon_{\rm bol}$ is the bolometric emissivity, for which we used $\varepsilon_{bol} = 0.95$ for all asteroids. The flux at a given wavelength (F_λ) is found by integrating the Planck function, B

Table A1
Observing Parameters for the SST Targets

Object	Program ID	Date (UTC)	Time (UTC)	Exposure Time (s)				t_{AOR} (hr)	r (au)	Δ (au)	α (deg)
				SL2	SL1	LL2	LL1				
114 Kassandra	91	2004-Oct-20	14:43:15	29.36	12.58			0.176	2.487	2.355	24.1235
234 Barbara	91	2005-Sep-12	9:52:28	29.36	12.58	12.58	12.58	0.132	1.967	1.598	31.2969
5261 Eureka	465	2007-Dec-08	7:31:16	365.70	365.70	377.52	755.04	0.706	1.445	0.704	40.4312
85989 1999 JD$_6$	40322	2008-Jun-04	12:29:34		264.24			0.14	1.072	0.336	70.3578

Note. t_{AOR} is the total observing time, r is the heliocentric distance, Δ is the SST–asteroid distance, and α is the SST-centered phase angle. For time-specific parameters, values are given for the start of each observation.

Table A2
Physical Parameters Derived from the NEATM

Object	H_v	R (km)	p_v	η	T_{SS} (K)	Parameters Derived from WISE[a]		
						R (km)	p_v	η
114 Kassandra	8.51	$49.56^{+1.76}_{-1.84}$	$0.070^{+0.009}_{-0.010}$	$0.93^{+0.01}_{-0.01}$	$256.0^{+0.6}_{-0.9}$	49.58 ± 1.59	0.09 ± 0.01	0.98 ± 0.09
234 Barbara	9.15	$22.55^{+0.82}_{-0.81}$	$0.190^{+0.026}_{-0.030}$	$1.09^{+0.02}_{-0.02}$	$273.1^{+1.2}_{-1.0}$	22.74 ± 0.125	0.21 ± 0.03	0.84 ± 0.01
5261 Eureka	16.13	$1.20^{+0.04}_{-0.04}$	$0.108^{+0.010}_{-0.011}$	$1.03^{+0.03}_{-0.02}$	$325.7^{+1.9}_{-1.4}$	0.78 ± 0.15	0.20 ± 0.10	0.95 ± 0.19
85989 1999 JD$_6$	17.12	$0.92^{+0.03}_{-0.04}$	$0.074^{+0.028}_{-0.043}$	$1.72^{+0.03}_{-0.06}$	$333.6^{+1.1}_{-2.5}$	0.80 ± 0.30	0.11 ± 0.17	1.40 ± 0.45

Note.
[a] Data from the Wide-field Infrared Survey Explorer (WISE; E. L. Wright et al. 2010) for Kassandra and Barbara are from J. R. Masiero et al. (2014), and data for Eureka and 1999 JD$_6$ are from C. R. Nugent et al. (2016).

---

[5] https://irsa.ipac.caltech.edu/applications/Spitzer/SHA/

[6] https://ssd.jpl.nasa.gov/horizons/app.html#/

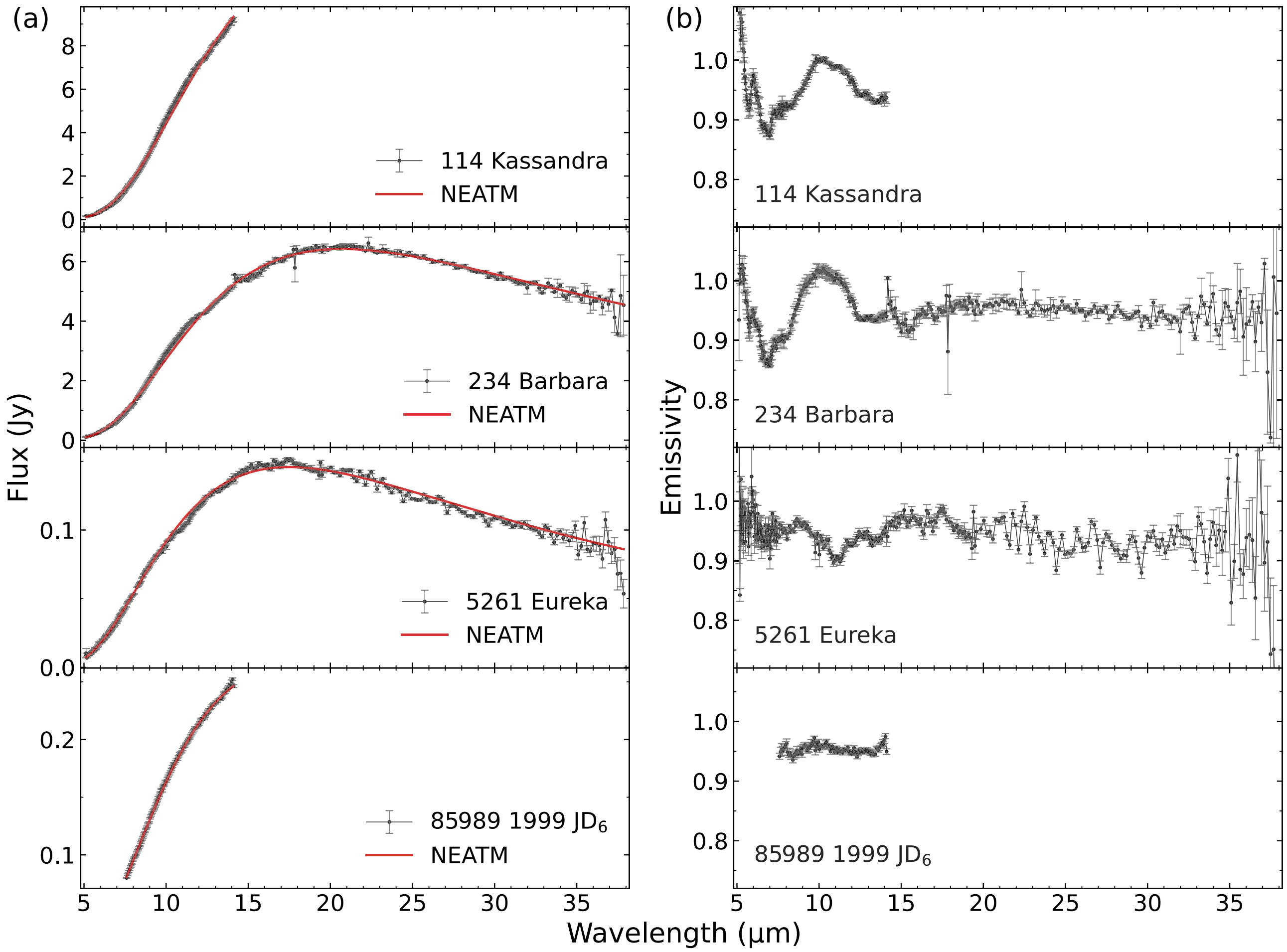

Figure A1. SEDs of the asteroids from this study observed by the SST. (a) The flux of each asteroid (black solid line with points) and its best-fit NEATM (red solid line). (b) Emissivity (i.e., $\varepsilon_{\mathrm{bol}}$SED/NEATM) of each asteroid.

(λ, T), over the dayside hemisphere of the asteroid:

$$F_\lambda = \frac{1}{\Delta^2}\int \varepsilon_{\mathrm{bol}} B(\lambda, T)\cos\theta_e dA, \quad \text{(A2)}$$

where Δ is the SST–asteroid distance, and θ_e is the emission angle. We varied A_B and η in Equation (A1) to vary T_{SS}, inputted the resulting T_{SS} into Equation (A2), and performed a χ^2 test between the observed flux (from SST) and the modeled flux (F_λ) to find the best-fit model. p_v is related to A_B by $A_B = p_v(0.290 + 0.684G)$, where G is the slope parameter (E. Bowell et al. 1989; J. W. Fowler & J. R. Chillemi 1992). We used a value of $G = 0.15$ for Barbara and Kassandra (J. R. Masiero et al. 2014), and $G = 0.24$ for Eureka and 1999 JD$_6$ (C. R. Nugent et al. 2016). R is then derived from the expression from J. W. Fowler & J. R. Chillemi (1992):

$$2R = \frac{1329}{\sqrt{p_v}}10^{-H_v/5}, \quad \text{(A3)}$$

where H_v is the absolute visual magnitude (obtained from JPL Horizons at the time of each observation). Finally, we calculated the emissivity spectrum for each asteroid by dividing the SED by the best-fit NEATM model, all multiplied by $\varepsilon_{\mathrm{bol}}$ (Figure A1).

ORCID iDs

Lonnie D. Dausend https://orcid.org/0009-0004-0200-1100
Audrey C. Martin https://orcid.org/0000-0003-3402-1339
Joshua P. Emery https://orcid.org/0000-0001-9265-9475

References

Alexander, C. M. O. D., Fogel, M., Yabuta, H., & Cody, G. D. 2007, GeCoA, 71, 4380

Beck, P., Garenne, A., Quirico, E., et al. 2014, Icar, 229, 263

Bell, J. F. 1988, Metic, 23, 256

Binzel, R. P., Harris, A. W., Bus, S. J., & Burbine, T. H. 2001, Icar, 151, 139

Binzel, R. P., DeMeo, F. E., Turtelboom, E. V., et al. 2019, Icar, 324, 41

Bland, P. A., Cressey, G., & Menzies, O. N. 2004, M&PS, 39, 3

Bowell, E., Hapke, B., Domingue, D., et al. 1989, in Proc. of the Conf. Asteroids II, ed. R. P. Binzel, T. Gehrels, & M. S. Matthews (Tucson, AZ: Univ. Arizona Press), 524

Bramble, M. S., Milliken, R. E., & Patterson, W. R. I. 2021a, Icar, 369, 114251

Bramble, M. S., Milliken, R. E., & Patterson, W. R. I. 2021b, Icar, 369, 114561

Brucato, J. R., Strazzulla, G., Baratta, G., & Colangeli, L. 2004, A&A, 413, 395

Bus, S. J., & Binzel, R. P. 2002, Icar, 158, 146

Chihara, H., Koike, C., Tsuchiyama, A., Tachibana, S., & Sakamoto, D. 2002, A&A, 391, 267

Clark, B. E., Ockert-Bell, M. E., Cloutis, E. A., et al. 2009, Icar, 202, 119

Clark, R. N., & Roush, T. L. 1984, JGR, 89, 6329

Clarke, R. S. J., Jarosewich, E., Mason, B., et al. 1971, SmCES, 5, 1

Cloutis, E. A., Hudon, P., Hiroi, T., et al. 2012, Icar, 221, 328

Dausend, L. D., Martin, A. C., & Emery, J. P. 2024, Measuring the effects of regolith porosity on mid-IR spectra of the Allende meteorite, v1.0, Zenodo, doi:10.5281/zenodo.12808383

de León, J., Licandro, J., Serra-Ricart, M., Pinilla-Alonso, N., & Campins, H. 2010, A&A, 517, A23
DeMeo, F. E., Binzel, R. P., Slivan, S. M., & Bus, S. J. 2009, Icar, 202, 160
DeMeo, F. E., Burt, B. J., Marsset, M., et al. 2022, Icar, 380, 114971
Devogèle, M., Tanga, P., Cellino, A., et al. 2018, Icar, 304, 31
Donaldson Hanna, K. L., Bowles, N. E., Warren, T. J., et al. 2021, JGRE, 126, e06624
Donaldson Hanna, K. L., Greenhagen, B. T., Patterson, W. R., et al. 2017, Icar, 283, 326
Donaldson Hanna, K. L., Schrader, D. L., Cloutis, E. A., et al. 2019, Icar, 319, 701
Donaldson Hanna, K. L., Wyatt, M. B., Thomas, I. R., et al. 2012, JGRE, 117, E00H05
Dotto, E., Barucci, M. A., Müller, T. G., et al. 2002, A&A, 393, 1065
Emery, J. P., Burr, D. M., & Cruikshank, D. P. 2011, AJ, 141, 25
Emery, J. P., Cruikshank, D. P., & Van Cleve, J. 2006, Icar, 182, 496
Eschrig, J., Bonal, L., Beck, P., & Prestgard, T. J. 2021, Icar, 354, 114034
Fowler, J. W., & Chillemi, J. R. 1992, IRAS Asteroid Data Processing, The IRAS Minor Planet Survey, Technical Report PL-TR-92-2049, Phillips Laboratory, Hanscom AF Base, MA, https://irsa.ipac.caltech.edu/IRASdocs/surveys/PL-TR-92-2049.pdf
Gail, H. P. 2004, A&A, 413, 571
Gomez Barrientos, J., de Kleer, K., Ehlmann, B. L., Tissot, F. L. H., & Mueller, J. 2024, ApJL, 967, L11
Greenwood, R. C., Burbine, T. H., & Franchi, I. A. 2020, GeCoA, 277, 377
Grossman, L. 1975, GeCoA, 39, 433
Hamilton, V. E. 2000, JGR, 105, 9701
Hamilton, V. E. 2010, ChEG, 70, 7
Harris, A. W. 1998, Icar, 131, 291
Henning, T. 2010, ARA&A, 48, 21
Houck, J. R., Roellig, T. L., van Cleve, J., et al. 2004, ApJS, 154, 18
Howard, K. T., Benedix, G. K., Bland, P. A., & Cressey, G. 2010, GeCoA, 74, 5084
Hunt, G. R., & Logan, L. M. 1972, ApOpt, 11, 142
Izawa, M. R. M., King, P. L., Vernazza, P., Berger, J. A., & McCutcheon, W. A. 2021, Icar, 359, 114328
Kessler, M. F., Steinz, J. A., Anderegg, M. E., et al. 1996, A&A, 315, L27
Koike, C., Chihara, H., Tsuchiyama, A., et al. 2003, A&A, 399, 1101
Kornacki, A. S., & Wood, J. A. 1984, GeCoA, 48, 1663
Kuroda, D., Ishiguro, M., Naito, H., et al. 2021, A&A, 646, A51
Lane, M. D., Glotch, T. D., Dyar, M. D., et al. 2011, JGRE, 116, E08010
Lantz, C., Brunetto, R., Barucci, M. A., et al. 2017, Icar, 285, 43
Lebofsky, L. A., & Spencer, J. R. 1989, in Proc. of the Conf. Asteroids II, ed. R. P. Binzel, T. Gehrels, & M. S. Matthews (Tucson, AZ: Univ. Arizona Press), 128
Licandro, J., Hargrove, K., Kelley, M., et al. 2012, A&A, 537, A73
Lim, L. F., Emery, J. P., & Moskovitz, N. A. 2011a, Icar, 213, 510
Lim, L. F., Emery, J. P., Mueller, M., et al. 2011b, in EPSC-DPS Joint Meeting 2011, 1199
Lord, H. C. I 1965, Icar, 4, 279
Lowry, V. C., Donaldson Hanna, K. L., Campins, H., et al. 2022, E&SS, 9, e02146
Macke, R. J., Consolmagno, G. J., & Britt, D. T. 2011, MAPS, 46, 1842
Mahlke, M., Eschrig, J., Carry, B., Bonal, L., & Beck, P. 2023, A&A, 676, A94
Marchis, F., Enriquez, J. E., Emery, J. P., et al. 2012, Icar, 221, 1130
Martin, A. C., & Emery, J. P. 2023, PSJ, 4, 153
Martin, A. C., Emery, J. P., Loeffler, M., & Donaldson Hanna, K. L. 2025, PSJ, submitted
Martin, A. C., Emery, J. P., & Loeffler, M. J. 2022, Icar, 378, 114921
Martin, A. C., Emery, J. P., & Loeffler, M. J. 2023, Icar, 397, 115507
Marvin, U. B., Wood, J. A., & Dickey, J. S. 1970, E&PSL, 7, 346
Masiero, J. R., Grav, T., Mainzer, A. K., et al. 2014, ApJ, 791, 121
McAdam, M. M., Sunshine, J. M., Howard, K. T., & McCoy, T. M. 2015, Icar, 245, 320
McCord, T. B., Adams, J. B., & Johnson, T. V. 1970, Sci, 168, 1445
McSween, H. Y., Binzel, R. P., de Sanctis, M. C., et al. 2013, MAPS, 48, 2090
McSween, H. Y. J. 1977, GeCoA, 41, 1777
Morlok, A., Schiller, B., Weber, I., et al. 2020, P&SS, 193, 105078
Mothé-Diniz, T., Carvano, J. M., Bus, S. J., Duffard, R., & Burbine, T. H. 2008, Icar, 195, 277
Müller, W. F., Weinbruch, S., Walter, R., & Müller-Beneke, G. 1995, P&SS, 43, 469
Mustard, J. F., & Hays, J. E. 1997, Icar, 125, 145
Nugent, C. R., Mainzer, A., Bauer, J., et al. 2016, AJ, 152, 63
Ramsey, M. S., & Christensen, P. R. 1998, JGR, 103, 577
Rayner, J. T., Toomey, D. W., Onaka, P. M., et al. 2003, PASP, 115, 362
Rivkin, A. S., Howell, E. S., & Emery, J. P. 2019, JGRE, 124, 1393
Rivkin, A. S., Trilling, D. E., Thomas, C. A., et al. 2007, Icar, 192, 434
Salisbury, J. W., D'Aria, D. M., & Jarosewich, E. 1991, Icar, 92, 280
Salisbury, J. W., & Eastes, J. W. 1985, Icar, 64, 586
Salisbury, J. W., & Wald, A. 1992, Icar, 96, 121
Sanchez, J. A., Reddy, V., Kelley, M. S., et al. 2014, Icar, 228, 288
Shirley, K. A., & Glotch, T. D. 2019, JGRE, 124, 970
Shirley, K. A., Glotch, T. D., Donaldson, O., et al. 2023, JGRE, 128, e2022JE007629
Sultana, R., Poch, O., Beck, P., et al. 2023, Icar, 395, 115492
Sunshine, J. M., Connolly, H. C., McCoy, T. J., Bus, S. J., & La Croix, L. M. 2008, Sci, 320, 514
Tamanai, A., Mutschke, H., Blum, J., & Meeus, G. 2006, ApJL, 648, L147
Trilling, D. E., Rivkin, A. S., Stansberry, J. A., et al. 2007, Icar, 192, 442
van der Velden, E. 2020, JOSS, 5, 2004
Vernazza, P., Carry, B., Emery, J., et al. 2010, Icar, 207, 800
Vernazza, P., Castillo-Rogez, J., Beck, P., et al. 2017, AJ, 153, 72
Vernazza, P., Delbo, M., King, P. L., et al. 2012, Icar, 221, 1162
Werner, M. W., Roellig, T. L., Low, F. J., et al. 2004, ApJS, 154, 1
Wright, E. L., Eisenhardt, P. R. M., Mainzer, A. K., et al. 2010, AJ, 140, 1868
Yang, B., Lucey, P., & Glotch, T. 2013, Icar, 223, 359
Young, C. L., Poston, M. J., Wray, J. J., Hand, K. P., & Carlson, R. W. 2019, Icar, 321, 71